Journal of Materials Chemistry A

REVIEW

View Article Online
View Journal | View Issue

Cite this: J. Mater. Chem. A, 2026, 14, 4870

Chalcogen cathodes beyond sulfur: the rising role of selenium and tellurium in zinc-ion energy storage

Hiren K. Machhi and Jiří Červenka *

Aqueous zinc-ion batteries are gaining increasing attention as next-generation energy storage systems due to their inherent safety, cost-effectiveness, and environmental compatibility. Yet, the limited availability of high-performance cathode materials continues to constrain their practical development. Chalcogen-based materials, particularly selenium (Se) and tellurium (Te), have recently emerged as promising cathode candidates due to their high volumetric capacities, multi-electron redox chemistries, and superior electrical conductivities compared with sulfur and conventional oxide materials. This review summarizes recent advances in the design, synthesis, and electrochemical performance of Se- and Te-based cathodes for aqueous zinc-ion batteries. We discuss how their fundamental physicochemical properties, electronic structures, and redox mechanisms in aqueous electrolytes govern energy storage behaviour. Particular emphasis is placed on structure–property relationships, including nanoscale engineering, conductive host confinement, and interfacial modulation, which stabilize redox reactions and enhance capacity retention. Comparative analyses with other cathode families highlight both the advantages and persistent limitations of chalcogen-based cathodes. Finally, we outline future directions for the rational design of advanced Se- and Te-based cathodes, to improve their energy density and durability. We provide a comprehensive perspective on the emerging role of Se and Te in aqueous zinc-ion batteries, focusing on their ability to drive high-performance, safe, and practical energy storage solute ions.

Received 7th October 2025
Accepted 13th December 2025

DOI: 10.1039/d5ta08186f

rsc.li/materials-a

Introduction

With the shift toward renewable energy, there is a growing interest in energy storage systems that are safe, affordable, and efficient. Although lithium-ion batteries currently lead the

Department of Thin Films and Nanostructures, Institute of Physics of the Czech Academy of Sciences (FZU), Prague 6, 162 00, Czech Republic. E-mail: machhi@fzu.cz; cervenka@fzu.cz

Hiren K. Machhi

Hiren K. Machhi is currently a Postdoctoral Research Fellow at the Institute of Physics of the Czech Academy of Sciences (FZU), Prague, Czech Republic. He received his doctoral degree from Sardar Patel University, Gujarat, India, in 2023, where he worked on polymer electrolytes, organic ionic conductors, and MOFs for zinc-ion batteries. His research involves the development and characterization of electrode materials and aqueous polymer electrolytes to enhance the electrochemical performance of zinc-ion batteries.

Jiří Červenka

Jiří Červenka is a Senior Scientist at the Institute of Physics of the Czech Academy of Sciences (FZU) in Prague, Czech Republic. He received his PhD from Eindhoven University of Technology in 2009. From 2011 to 2015, he was a Research Fellow in the Faculty of Science at the University of Melbourne. His research focuses on the fundamental mechanisms governing nanomaterials and electrochemical energy-storage systems. His group develops functionalized electrode materials and advanced electrolytes for aqueous batteries and next-generation lithium-ion battery technologies.

market, their dependence on limited resources, elevated costs, and safety concerns restricts broad-scale deployment.[1] Aqueous zinc-ion batteries (AZIBs) represent a compelling alternative energy storage technology in the quest for systems "beyond lithium-ion batteries".[2] Aqueous electrolytes are inherently safe, non-flammable, while enabling fast ion transport. Zinc is abundant, inexpensive, and environmentally benign. Beyond sustainability, AZIBs present unique electrochemical advantages. Zinc's divalent nature provides high theoretical specific capacity (820 mA h g^{-1}), low redox potential (−0.76 V *vs.* SHE), and zinc metal anodes simplify cell design and reduce manufacturing complexity. However, these benefits are offset by significant materials challenges, such as sluggish zinc-ion diffusion, dendrite formation at the anode, cathode structural instability, and parasitic reactions in aqueous environments, all of which conspire to limit energy density, rate capability, and long-term cycling stability. Therefore, realizing the full potential of AZIBs remains a formidable challenge.

The performance of AZIBs is mainly determined by the synergistic interplay of their core components: the anode, cathode, and electrolyte. Zinc metal foil, commonly used as the anode, is prone to dendritic growth, unwanted hydrogen evolution reaction (HER), and corrosion. These problems critically affect both the safety and operational longevity of the battery, manifesting as short-circuit failures, capacity decline, and overall performance loss. AZIBs typically involve aqueous electrolytes based on zinc sulfate ($ZnSO_4$), zinc trifluoromethanesulfonate ($Zn(CF_3SO_3)_2$, ZnTFS) and zinc chloride salts. However, key to their performance is the development of advanced cathode materials capable of reversible Zn^{2+} insertion/extraction and which can facilitate multi-electron transfer reactions. Addressing these issues requires a deep understanding of cathode chemistry, interfacial engineering, electrolyte formulation, and conversion mechanisms. Despite increasing research efforts, a comprehensive mechanistic understanding of AZIB operation remains incomplete, particularly regarding multi-electron cathode processes, zinc/proton co-intercalation, and solid–liquid phase transitions. Bridging these knowledge gaps is critical not only to optimize device performance but also to unlock the full potential of AZIBs as next-generation, safe, and sustainable energy storage solutions for grid-scale and portable applications.

A wide range of cathode materials has been explored in AZIBs over the years, including manganese- and vanadium-based materials, Prussian blue compounds, organic compounds, 2D materials, and chalcogens.[3] Manganese-based cathodes are particularly promising for aqueous zinc-ion batteries owing to their low cost, natural abundance, environmental compatibility, and structural diversity, which enable fast Zn^{2+} diffusion and a relatively high theoretical capacity.[4] In comparison, vanadium-based cathodes provide higher specific capacities and improved reversibility, benefiting from multiple oxidation states and layered frameworks with large interlayer spacing that support both Zn^{2+} insertion and proton co-storage.[5] Prussian blue analogues (PBAs) feature an open three-dimensional framework and relatively high operating voltage. However, their practical application is hindered by structural instability, often resulting in framework collapse, capacity fading, and performance degradation during cycling.[6] Organic cathode materials have also been examined, but their progress is constrained by complex synthesis routes and vulnerability to side reactions that undermine their long-term stability and practical viability.[7]

Halide-based compounds are also considered as promising conversion-type cathode materials in zinc-based energy storage, owing to their unique redox chemistry and fast reaction kinetics. Unlike traditional intercalation cathodes, halogen-based systems such as iodine (I_2), bromine (Br_2), and chlorine (Cl_2) are reversibly converted at the cathode through oxidation–reduction reactions, while Zn^{2+} is reversibly plated and stripped at the anode.[8] Iodine cathodes offer reversible I_2/I^- conversion and excellent rate performance, but suffer from severe polyiodide dissolution. This issue is commonly addressed by confining iodine within porous carbon or polymer hosts to enhance cycling stability.[9] Bromine-based systems exhibit even faster kinetics and higher power capability owing to their liquid-phase Br_2/Br^- redox chemistry. However, their volatility and crossover issues necessitate effective stabilization strategies, such as gel electrolytes and host–guest confinement.[10] Chlorine cathodes possess the highest theoretical energy among halogens, yet their practical use is limited by their high reactivity and gaseous nature of Cl_2. Recent efforts therefore focus on encapsulation and solid-state chloride frameworks to improve safety and reversibility.[11] However, halide cathodes are prone to polyhalide formation and dissolution, shuttle effects, volatility, and high reactivity. These issues collectively reduce coulombic efficiency and shorten the cycling life of zinc-halide batteries.[12] To address these limitations, recent strategies include the confinement of halogen species within porous carbon frameworks, MOFs/COFs, or polymer matrices, the implementation of host–guest complexation, and the development of solid-state electrolytes. These approaches enhance redox reversibility, stabilize the active material, and improve the long-term durability and overall electrochemical performance of zinc–halide batteries.

Despite these progresses, the development of robust cathode materials for AZIBs remains fraught with fundamental challenges. The sluggish Zn^{2+} kinetics caused by strong electrostatic interactions, structural collapse, active material dissolution, and irreversible volume changes collectively contribute to capacity fading and poor cycling stability. Additionally, many cathodes suffer from low electrical conductivity, side reactions in aqueous electrolytes, and poor rate capability. All of these aspects restrict their overall performance and practical applications.[13]

Recently, conversion-type chalcogen cathodes, based on sulfur (S), selenium (Se), and tellurium (Te), have emerged as a highly promising alternative strategy. These materials offer distinct advantages over conventional insertion-type cathodes, including natural abundance, exceptionally high specific capacity, and superior power density.[14] The attainment of multielectron transfer reactions in such elements has the potential to substantially enhance the energy density of AZIBs.[15]

The key physicochemical properties of S, Se, and Te are summarized in Fig. 1.

Over the last few years, a growing number of AZIBs have been developed that utilize chalcogen elements (S, Se, and Te) as cathode materials, revealing diverse reaction mechanisms.[17] Among them, zinc–sulfur (Zn–S) batteries have been most extensively studied. Sulfur, owing to its high theoretical capacity (1675 mA h g^{-1}) and natural abundance, represents a low-cost and environmentally friendly cathode candidate. At the heart of sulfur's electrochemistry lies a multi-electron conversion process that drives its remarkable capacity. Elemental sulfur (S_8) undergoes a multi-electron conversion reaction with Zn^{2+} ions during electrochemical cycling to form zinc polysulfides (ZnS_x, $x = 1$–8), ultimately producing ZnS as the fully discharged product.[18] Despite these advantages, sulfur cathodes face several persistent challenges due to sulfur's poor electrical conductivity and the dissolution of intermediate polysulfides into the aqueous electrolyte, which results in capacity fading, limited rate performance, and reduced cyclic stability. The other chalcogen elements (Se and Te) also exhibit multielectron transfer reactions, offering the potential for ultrahigh specific capacities. This has spurred growing interest in conversion-type chalcogen cathodes, which have garnered significant attention in the scientific community over the past few years.

Recent studies have increasingly focused on the electrochemical behaviour and reaction mechanism in conversion batteries using S, Se, and Te cathodes. Zhao *et al.* reviewed the electrochemical behaviour and recent progress of sulfur-based aqueous batteries, summarizing key insights into reaction mechanisms and performance evolution of sulfur-based cathodes.[19,20] However, comparable reviews addressing selenium- and tellurium-based cathodes remain scarce. This gap in the current understanding underscores the need for a dedicated assessment that systematically summarizes recent advances in Se and Te cathode materials and elucidates their underlying electrochemical mechanisms in AZIBs.

To address this gap, this review systematically summarizes recent advances in AZIBs employing selenium (Se) and tellurium (Te) based cathode materials. We elucidate the underlying reaction mechanisms governing their energy storage mechanism and associated challenges with the multielectron transfer reactions. Additionally, we discuss current strategies aimed at improving electrode design, enhancing reversibility, and mitigating dissolution and volume-change effects during cycling. Finally, the prospects and remaining challenges for Se/Te-based AZIBs are critically evaluated, with emphasis on providing targeted strategies to overcome each of these issues in future material development. By consolidating mechanistic insights and design strategies, this review provides a framework for the rational development of high-performance AZIBs based on conversion-type Se/Te cathodes.

Various cathode materials for ZIBs

Fig. 2 provides an overview of the representative crystal structures of cathode materials investigated for AZIBs. These materials span a wide range of structural chemistries, including manganese oxides, vanadium oxides and vanadates, Prussian blue analogues with open-framework architectures, as well as emerging cathode classes such as organic compounds, metal–organic frameworks, and chalcogen-based materials (sulfur, selenium and tellurium). Complementing this structural overview, Table 1 summarizes recently reported AZIB cathode materials, comparing their cathode reactions, charge-storage mechanisms, open-circuit voltages (OCVs), theoretical capacities, and energy densities.

Manganese oxide-based materials represent one of the most extensively investigated classes of cathode materials for AZIBs, due to their low cost, abundance, environmental friendliness, and rich redox chemistry involving multiple oxidation states. In particular, the Mn^{4+}/Mn^{3+} redox couple enables the delivery of high theoretical capacity (~308 mA h g^{-1} for MnO_2).[21] Manganese oxides exist in various polymorphic forms, including α-, β-, γ-, and δ-MnO_2, as well as todorokite, Mn_2O_3, Mn_3O_4, MnO, and $ZnMn_2O_4$, exhibiting tunnel, layered, and spinel structures capable of accommodating Zn^{2+} ion intercalation to varying extent.[22] In AZIBs, manganese oxide-based cathodes typically store Zn^{2+} ions through insertion-extraction (intercalation), co-insertion (H^+) in mildly acidic electrolytes, or conversion-type mechanisms. Among these, the layered δ-MnO_2 (birnessite-type) demonstrates particularly promising capacity due to its expanded interlayer spacing and water-assisted Zn^{2+} transport. Despite these advantages, manganese-based oxide cathodes are hindered by rapid capacity fading and poor rate performance. These issues primarily arise from structural degradation during

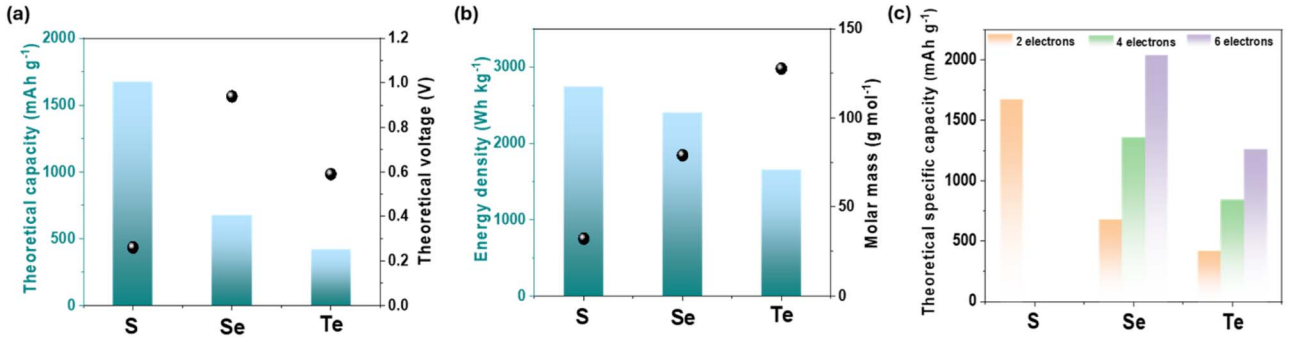

Fig. 1 Physicochemical properties of chalcogens (S, Se, and Te): (a) theoretical capacity, (b) energy density, and (c) theoretical specific capacity.[16]

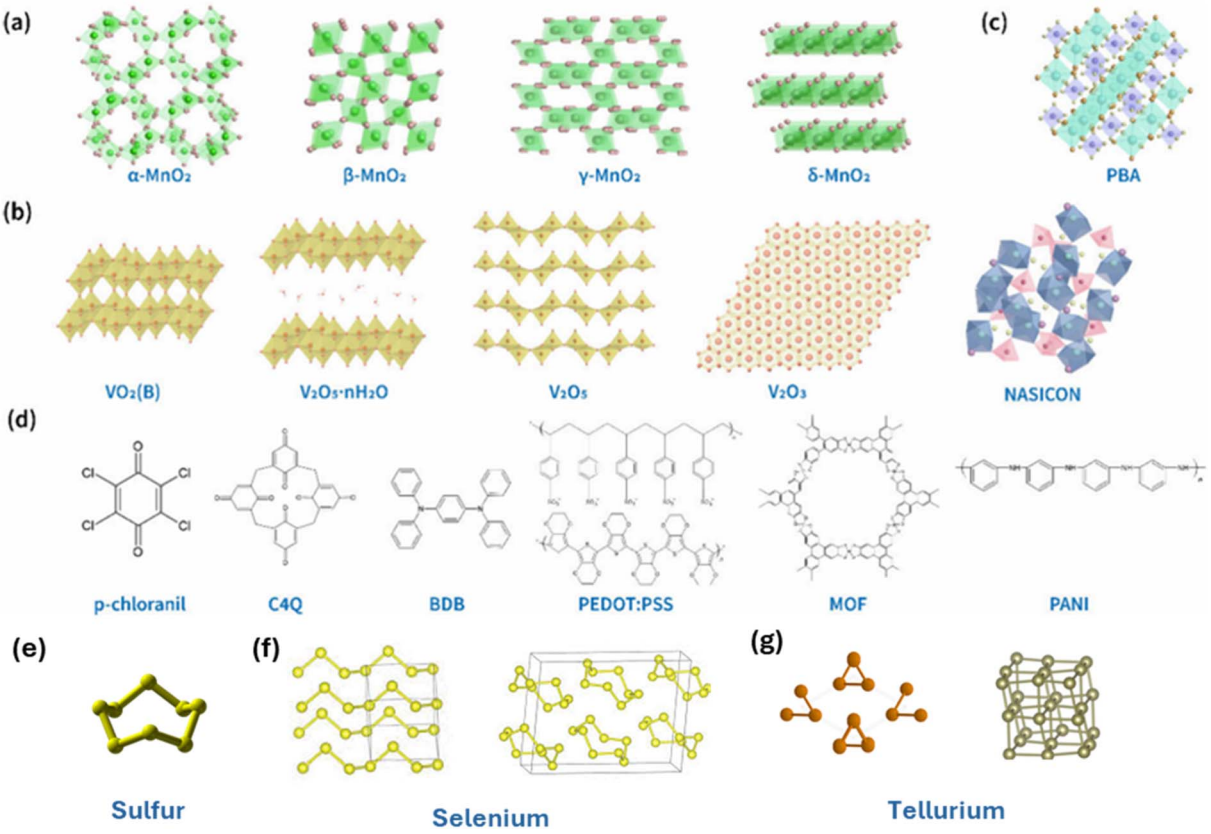

Fig. 2 Structures of various cathode materials for AZIBs: (a) manganese oxides, (b) vanadium oxides and vanadates, (c) Prussian blue analogues, (d) organic and metal–organic frameworks.[29] Reproduced from ref. 29 with permission from American Chemical Society, copyright 2025. Structures of (e) sulfur, (f) selenium, and (g) tellurium.

cycling, dissolution of manganese species into the electrolyte due to disproportionation reactions ($Mn^{3+} \rightarrow Mn^{2+} + Mn^{4+}$), and poor electronic conductivity. To mitigate these challenges, various strategies have been explored, including heteroatom doping, the use of nanocomposites with different morphologies and nanostructures (0D to 3D), surface modification, and optimization of the electrolyte. Such approaches have substantially improved cycling stability and reversibility of manganese oxide-based cathode systems.[23]

Vanadium oxide-based materials have also been widely studied as cathode materials, benefiting from rich redox chemistry, multiple valence states (V_x^+ (x = 2, 3, 4, 5)), and versatile structural frameworks. They feature open layered or tunnel structures that enhance Zn^{2+} ion accessibility and storage capacity. In the case of vanadium oxides, the basic V–O coordination polyhedra can adopt diverse geometries, ranging from tetrahedra, square pyramids, and trigonal bipyramids to distorted and regular octahedra. Such flexible structural configurations, along with variable oxidation states of vanadium, can be finely tuned to effectively accommodate Zn^{2+} ions and charge transfer behavior.[3] The hydrated vanadium pentoxide ($V_2O_5 \cdot nH_2O$) and vanadium bronzes (*e.g.*, $M_xV_2O_5$, where M = Na^+, K^+, NH_4^+) have also been widely explored because their interlayer water molecules and pre-inserted cations stabilize the frameworks and enhance ion mobility. Other vanadium oxides, such as VO_2, $V_3O_7 \cdot H_2O$, V_6O_{13}, V_2O_3, and $V_{10}O_{24} \cdot 12H_2O$, with mixed valency and tunable interlayer structures, have also demonstrated decent electrochemical performance.[24] In these systems, Zn^{2+} ions are generally stored through insertion/extraction processes. However, the sequence and transfer kinetics depend strongly on crystallographic polymorphs and interlayer spacing. Over the past few years of research, several studies have highlighted the possibility of a co-intercalation mechanism involving H^+ and Zn^{2+} ions, which may be responsible for the improved thermodynamics and kinetics. However, this mechanism remains a subject of ongoing investigation, and the position of inserted H^+ ions in the cathode and their impact on Zn^{2+} ion insertion still need to be validated. To further advance vanadium-based oxide materials, targeted strategies addressing structural instability, optimizing interlayer spacing, and resolving vanadium dissolution issues are required.

Other metal oxides and polyanionic compounds are another class of interesting cathode materials. Beyond Mn- and V-based oxide materials, several other transition metal oxide materials and polyanionic compounds have been investigated as cathodes for AZIBs. Although these materials show potential, their charge-storage mechanisms, structural evolution during cycling, and electrochemical performance require further exploration and clarification. Iron oxides (Fe_2O_3 and Fe_3O_4)

Table 1 Comparative table of cathode materials used in AZIBs

Cathode	Cathode reaction	Storage mechanism	~OCV(v) *vs.* Zn/Zn^{2+}	Theoretical capacity (mA h g^{-1})	Energy density (Wh kg^{-1})	Material cost
Manganese oxide-based cathodes						
α-MnO_2	$2MnO_2 + Zn^{2+} + 2e^- \rightarrow ZnMn_2O_4$	Zn^{2+} insertion	1.3–1.5	~308	~220–390	Low
δ-MnO_2	$MnO_2 + Zn^{2+} + e^- + H^+ \rightarrow Zn\ xMnO_2 \cdot H_2O$	Zn^{2+} & H^+ co-insertion	1.2–1.4	~308	~220–410	Low
γ-MnO_2	$MnO_2 + Zn^{2+} + e^- \leftrightarrow Zn \cdot xMnO_2$	Zn^{2+} insertion	1.1–1.3	~308	~220–390	Low
Mn_3O_4	$Mn_3O_4 + Zn^{2+} + 2e^- \rightarrow ZnMn_2O_4$	Conversion	1.0–1.2	~230	~120–320	Low
Vanadium-based oxide cathodes						
$V_2O_5 \cdot nH_2O$	$V_2O_5 \cdot nH_2O + xZn^{2+} + 2xe^- \leftrightarrow Zn_xV_2O_5 \cdot nH_2O$	Zn^{2+} & H^+ intercalation	0.8–1.1	~294	~180–450	Medium
$Zn_xV_2O_5$	Reversible de/intercalation of Zn^{2+}	Zn^{2+} intercalation	0.8–1.0	~300	~180–430	Medium
VO_2 (B-phase)	$VO_2 + Zn^{2+} + 2e^- \rightarrow ZnVO_2$	Zn^{2+} insertion	1.0–1.2	~300	~140–350	Medium
$Na_{0.3}V_2O_5 \cdot 1.5H_2O$	$Na_{0.3}V_2O_5 + xZn^{2+} + 2xe^- \leftrightarrow Zn_xNa_{0.3}V_2O_5$	Zn^{2+} intercalation (layered)	0.9–1.1	~280	~150–360	Medium
Other oxide materials and polyanionic cathodes						
MoO_3	$MoO_3 + xZn^{2+} + 2xe^- \leftrightarrow Zn_xMoO_3$	Zn^{2+} intercalation	~0.9–1.0	~279	~80–300	Medium
TiO_2 (anatase)	$TiO_2 + xZn^{2+} + 2xe^- \leftrightarrow Zn_xTiO_2$	Intercalation	~0.8–1.0	~170	~40–180	Low-medium
$NiCo_2O_4$	$NiCo_2O_4 + Zn^{2+} + e^- \rightarrow$ Zn–Ni–Co–O complex	Pseudocapacitive	~1.2	~250	~120–360	Medium
$Na_3V_2(PO_4)_3$	$Na_3V_2(PO_4)_3 + xZn^{2+} + 2xe^- \leftrightarrow Zn_xNa_3V_2(PO_4)_3$	Zn^{2+}/Na^+ intercalation	~1.2–1.4	~118	~80–150	High
$LiVPO_4F$	$LiVPO_4F + Zn^{2+} + 2e^- \leftrightarrow Zn_xLiVPO_4F$	Zn^{2+} insertion	~1.3	~140	~90–180	High
$KNaV(PO_4)_2$	$KNaV(PO_4)_2 + Zn^{2+} + 2e^- \leftrightarrow Zn_xKNaV(PO_4)_2$	Zn^{2+} intercalation	~1.0–1.2	~150	~60–150	Medium
Prussian blue analogues cathodes						
$Zn_3[Fe(CN)_6]_2$	$Fe^{3+} + e^- \leftrightarrow Fe^{2+}$ in open framework	Zn^{2+} intercalation in framework	~1.7–1.8	~60–70	~60–130	Low
CuHCF	$Cu^{3+} + e^- \leftrightarrow Cu^{2+}$	Zn^{2+} intercalation	~1.7–1.9	~70–75	~50–120	Low
MnHCF	$Mn^{3+} + e^- \leftrightarrow Mn^{2+}$	Zn^{2+} intercalation	~1.6–1.8	~60–80	~60–140	Low
Organic cathode materials						
AQDS (n-type)	$AQDS + 2e^- + 2H^+ \leftrightarrow AH_2QDS$	Proton-coupled redox reaction	~0.8–1.0	~224	~150–220	Low-medium
PANI (p-type)	PANI (ox) + $e^- \leftrightarrow$ PANI (red)	Zn^{2+} & H^+ doping/dedoping	~1.1–1.3	~180	~190–220	Low
Polyimides	–C═O redox centres + $Zn^{2+} + 2e^- \leftrightarrow$ –C–O–Zn	Zn^{2+} chelation	~1.0–1.2	~200–300	~190–310	Low-medium
Tetrahydroxybenzoquinone (THBQ)	THBQ + $Zn^{2+} + 2e^- \leftrightarrow$ Zn(THBQ)	Zn^{2+} coordination	~1.0	~390	~250–330	Low
MOF and COF cathode materials						
ZIF-8 derived Zn–C	Zn–MOF + $Zn^{2+} + 2e^- \rightarrow$ Zn intercalated composite	Intercalation/ Pseudocapacitive	~1.0–1.2	~250–300	~60–240	Medium
Co-MOF (*e.g.*, Co-BDC)	Co-MOF + $Zn^{2+} + e^- \rightarrow$ Zn inserted Co-MOF	Redox-active metal & ligand contribution	~1.2–1.4	~200–300	~80–280	Medium
Fe-BTC MOF	Fe-BTC + $Zn^{2+} + 2e^- \leftrightarrow$ Zn–Fe–BTC	Redox of Fe centers & coordination sites	~1.1	~220	~80–210	Medium
TpPa-1 COF	COF + $Zn^{2+} + 2e^- \rightarrow$ Zn-intercalated COF	Zn^{2+} coordination to carbonyl sites	~1.0–1.2	~250	~60–220	Medium
Phthalocyanine-COF	Pc-COF + $Zn^{2+} + 2e^- \rightarrow$ Zn–Pc-COF	Redox-active N atoms & conjugated π	~1.1	~200–300	~120–280	Medium
Quinone-linked COFs	COF + $Zn^{2+} + 2e^- \leftrightarrow$ Zn–COF	Redox of quinone groups	~1.0	~260–300	~130–280	Medium

Table 1 (*Contd.*)

Cathode	Cathode reaction	Storage mechanism	~OCV(v) *vs.* Zn/Zn^{2+}	Theoretical capacity ($mA\ h\ g^{-1}$)	Energy density ($Wh\ kg^{-1}$)	Material cost
Other emerging cathodes						
MoS_2 (TMD)	$MoS_2 + Zn^{2+} + 2e^- \leftrightarrow Zn_xMoS_2$	Zn^{2+} intercalation in layered TMD	~1.0–1.2	~220	~80–280	Medium
MXene (*e.g.*, Ti_3C_2)	Surface redox of –O/–OH sites	Pseudocapacitive storage	~1.0–1.2	~150–200	~110–180	Medium-high
Air (O_2)	$O_2 + 4e^- + 2H_2O \leftrightarrow 4OH^-$	ORR/OER on porous cathode	~1.6–1.8	—	—	Low
Halogen cathodes						
Iodine (I_2)	$I_2 + 2e^- \rightarrow 2I^-$	Surface redox (conversion)	~1.2–1.3	~211	~260–330	Medium
Bromine (Br_2)	$Br_2 + 2e^- \rightarrow 2Br^-$	Surface redox (conversion)	~1.8–1.9	~239	~120–320	Medium
Chlorine (Cl_2)	$Cl_2 + 2e^- \rightarrow 2Cl^-$	Surface redox (conversion)	~1.9–2.0	~229	~100–280	Low
Chalcogen cathodes						
Sulfur (S_8)	$S_8 + 16e^- + 16H^+ \rightarrow 8H_2S$ or $Zn + S \rightarrow ZnS$	Conversion to ZnS	~1.2–1.4	~1672	~300–720	Low
Selenium (Se)	$Se + 2e^- + Zn^{2+} \rightarrow ZnSe$	Conversion	~1.0–1.2	~678	~280–520	Medium
Tellurium (Te)	$Te + 2e^- + Zn^{2+} \rightarrow ZnTe$	Conversion	~0.9–1.1	~420	~240–500	High

have been reported to operate *via* H^+/Zn^{2+} co-insertion mechanism, while titanium oxides (TiO_2, $SrTiO_3$) involve insertion/se-insertion mechanism.[25] Nickel oxides, MoO_3, Co_3O_4, and Mn-doped ZnO employ an insertion/extraction mechanism.[25] Copper oxides (CuO, Cu_2O, and CuV_2O_6) have demonstrated diffusion-controlled kinetics and conversion.[25] In parallel, polyanionic compounds, particularly phosphates and fluorophosphates, have emerged as a distinct class of emerging AZIB cathodes. Owing to their intrinsically significant molar mass and strong interaction between P–O chemical bonds in phosphate groups, these materials often exhibit moderate specific capacities and high voltages.[3] The first polyanionic cathode for AZIBs was $Na_3V_2(PO_4)_3$, followed by carbon-coated $Na_3V_2(PO_4)_3$, Na_2FePO_4F, and $Na_3V_2(PO_4)_2F_3$ composite materials, which exhibited improved electronic conductivity and enhanced capacity.[26,27] The charge storage mechanism in these cathode materials demonstrates complex redox behaviour. It can involve Zn^{2+} intercalation or Na^+/Zn^{2+} co-intercalation, as observed in $Zn//Na_3V_2(PO_4)_3$ cells,[24] or a combined process where Zn^{2+} intercalation is accompanied by H^+ intercalation and deintercalation.[28]

Prussian Blue Analogues (PBAs) constitute a class of metal–organic framework-like compounds with a general formula $A_xM_1\ [M_2(CN)_6]_{1-y}\cdot nH_2O$, where A represents an alkali metal, M_1 and M_2 are transition metals, $0 < x < 2$, $y < 1$, and y is the amount of vacancies.[6] In these structures, M_1 and M_2 are coordinated through N and C of the CN ligand, forming a three-dimensional open M_1–N≡C–M_2 chain structure acting as reversible storage sites for Zn^{2+} ions.[6] The nanoporous architecture, combined with the redox-active M_1 and M_2 metal centres embedded within the PBA lattice, has captivating applicability in electrochemical energy storage systems. In AZIBs, PBAs primarily involve reversible Zn^{2+} ion intercalation/de-intercalation coupled with H^+ co-insertion, accompanied by redox reactions at transition metal centres (typically Fe^{2+}/Fe^{3+}). This mechanism yields a relatively high operating voltage of 1.5 to 1.8 V.[30] Despite these advantages, PBAs face several challenges, such as structural defects, poor conductivity, and framework degradation in harsh aqueous electrolytes. To overcome these issues, recent strategies have focused on defect control during synthesis, carbon compositing, core–shell structuring, and electrolyte optimization.

Organic materials have also emerged as promising cathode materials for AZIBs due to their structural tunability, sustainability, and compatibility with green chemistry approaches.[31] These materials typically contain redox-active functional groups, such as carbonyls, quinones, imines, or nitroxides, which can undergo reversible electron transfer during charge–discharge cycling.[31] This differs fundamentally from the traditional intercalation/de-intercalation mechanism. Based on their redox characteristics, the organic molecules are broadly classified into n-type, p-type and bipolar subclasses. (1) n-type organic molecules undergo reduction (by accepting electrons) during discharge and coordinating with Zn^{2+} or H^+ ions and releasing them during charge. The examples of n-type organic molecules include quinone-based compounds like anthraquinone, benzoquinone and anthraquinone-2,7-disulfonic acid (AQDS),

where carbonyl groups serve as active sites for reversible Zn^{2+} or H^+ coordination and electron transfer. (2) In contrast, p-type organic molecules like polyaniline (PANI) and polypyrrole (PPy) and Polythiophene undergo oxidation (by donating electrons) during the discharge process, allowing anion insertion from the electrolyte into their structure, which are subsequently expelled upon charging. (3) Bipolar organic compounds, including dihydro-octaaza-pentacene (DOP) and indanthrone, combine both n-type and p-type redox sites, allowing for multi-electron transfer processes that store both cations and anions, thereby resulting in significantly higher capacities.[32,33]

Metal/Covalent Organic Frameworks (MOFs/COFs) have recently attracted growing interest as cathode materials due to their tunable porosity, large surface areas, and structural versatility. MOFs are composed of metal ions or clusters coordinated with organic ligands, forming crystalline networks that facilitate Zn^{2+} ion diffusion and storage. Although pristine vanadium-, manganese-, and copper-based MOFs have been explored, their low electrical conductivity often limits their electrochemical performance. To overcome this, redox-active MOFs incorporating metal centres such as manganese, vanadium, or cobalt capable of reversible valence changes (*e.g.*, Mn^{3+}/Mn^{2+} or V^{5+}/V^{4+}) during Zn^{2+} insertion and extraction have been developed. In parallel, frameworks employing redox active organic linkers bearing carbonyl, imine, or phenazine groups have demonstrated dual-site charge-storage capability through both metal-centred and ligand-based redox processes.[34] In COFs, extended redox-active organic linkers are deliberately selected to introduce functional groups capable of reversible coordination with Zn^{2+} or H^+ ions.[35] Quinone-based linkers, such as anthraquinone and benzoquinone derivatives, offer carbonyl groups that undergo reversible redox reactions with Zn^{2+} ions. Imine-linked COFs, formed through Schiff-base reactions, provide nitrogen sites that can also contribute to redox activity, while phenazine, hydrazone, and perylene diimide-based linkers offer additional redox-active sites and extended conjugation, thereby enhancing both specific capacity and electronic conductivity.[35]

Transition metal dichalcogenides (TMDs) with the general formula of MX_2 (where M = Mo, Ti, V, W, *etc.*, and X = S, Se, or Te) comprise a family of layered materials consisting of a single layer of metal (M) atoms sandwiched between two layers of chalcogen (X) atoms. Their characteristic two-dimensional structure, held together by weak van der Waals interactions between layers, imparts excellent electronic and ionic transport properties.[36] The TMDs, such as MoS_2, VS_2, TiS_2, and VSe_2, have been extensively explored as cathodes for AZIBs due to their decent capacity, favourable intercalation/deintercalation chemistry, and ability to reversibly store Zn^{2+} ions. In some cases, co-intercalation of non-metallic carriers (H^+ and NH_4^+) along with Zn^{2+} ion has also been reported in some TMDs, effectively utilizing a higher number of active sites and enhancing reversible capacity and cycling life.[37]

Layered double hydroxides (LDHs) represent another important class of two-dimensional transition metal-based materials, generally described by the formula of $[M_{1-x}^{2+}M_x^{3+}(OH)_2]^{x+}(A^{n-})_{x/n}\cdot y\ H_2O$, where M^{2+} and M^{3+} denote divalent and trivalent metal cations, and A^{n-} represents the related interlayer anion, with x representing the ratio of $M^{3+}/(M^{2+} + M^{3+})$, where $(0.1 < x < 0.5)$.[38] The alternating positively charged metal hydroxide layers and negatively charged anionic sheets are stabilized by electrostatic interactions, creating a lamellar architecture with large surface area and abundant active sites for Zn^{2+} intercalation. To date, a variety of LDHs, including CoNi, FeCO, CoMn, ZnCO, *etc*, have been synthesized and applied in AZIBs. Additionally, composite and doped variants of LDHs, such as $CoNiTi_3C_2$, $CoNi@NiCo_2S_4$, CoNi@GO, $CoNi@CoSe_2$, and Zn-LDHs@MXene, have been reported, demonstrating superior ionic diffusion and electrical conductivity, translating to high capacity and enhanced cyclic stability in zinc storage systems.[39]

MXenes, a broad class of 2D transition metal carbides, nitrides, and carbonitrides with the general formula $M_{n+1}X_nT_x$ (n = 1 to 4), where M represents a transition metal and T_x represents surface terminal groups (such as –O, –OH, –F, or –Cl), have also shown great potential as cathodes and conductive hosts in AZIBs.[40] MXenes exhibit excellent electrical conductivity, and their rich hydrophilic functional groups on the surface grant them good electrolyte wettability. They also have a large surface area, open interlayer spacing, and surface functionalities that facilitate fast ion diffusion and redox reactions, making them suitable for excellent energy storage applications. Recent studies on $Ti_3C_2T_x$ and composites of $Ti_3C_2T_x$ with polyaniline (PANI) or vanadium oxide (VO_2) have demonstrated promising zinc ion storage *via* intercalation–deintercalation mechanisms.[41]

Halogens-based systems, particularly iodine, bromine, and chlorine, have emerged as interesting classes of cathode chemistries in zinc-halogen batteries. These materials combine high theoretical capacities, favourable redox potentials, fast redox kinetics, and intrinsic safety with cost-effectiveness.[42] For instance, Zn–I_2 systems exhibit theoretical capacities of 211 mA h g^{-1} (I^-/I^0), 422 mA h g^{-1} (I^-/I^+), and up to 1200 mA h g^{-1} (I^-/IO_3^-), while Zn–Br_2 and Zn–Cl_2 systems deliver 335 and 755 mA h g^{-1}, respectively.[42] Yet, the halogen volatility, corrosiveness, and crossover issues pose major barriers to practical deployment.

Air, particularly the oxygen element used as a sustainable cathode material in zinc–air batteries, represents a distinct category within zinc-based energy storage technologies. Unlike conventional cathodes, this system utilizes ambient oxygen as a cathode reactant, which diffuses into the air electrode where it undergoes electrochemical reduction. During discharge, typically in an alkaline medium, this process forms hydroxide ions, resulting in the overall formation of zincate or zinc oxide.[43] The oxygen reduction reaction (ORR) at the cathode is the key step that essentially defines battery efficiency. To enhance the ORR kinetics, a wide range of catalysts including metal catalysts (such as platinum and its Pt–Co, Pt–Ni alloys), transition metal oxides (such as MnO_2, Co_3O_4, $NiCo_2O_4$ and Fe_3O_4), carbon-based materials (such as nitrogen-doped graphene, carbon nanotubes, and activated carbon) and emerging single-atom catalysts and metal–nitrogen–carbon (M–N–C) complexes have been developed.[44]

Sulfur has also been investigated as a promising cathode material for zinc-based batteries owing to its natural abundance, low costs, and high theoretical capacity. Sulfur undergoes a two-electron solid-state redox reaction involving interconversion between S^0/S^{2-} delivering huge theoretical capacity (~1675 mA h g^{-1}), but suffering from volume expansion, poor electrical conductivity, sluggish reaction kinetics, and polysulfide species formation causing capacity fading.[45] To address these challenges, researchers have incorporated sulfur into conductive carbon hosts, including graphene, carbon nanotubes, and porous carbon frameworks. The use of catalytic additives (*e.g.*, MnO_2, CoS), electrolyte engineering, and functional separators has also been explored to enhance redox kinetics and confine polysulfide intermediates.[46] Although Zn–S batteries are still in the early stages of development, continued progress in material design and interfacial engineering is expected to accelerate their path toward practical applications.

Zinc–selenium (Zn–Se) batteries

Selenium (Se), an element of group 16 in the chalcogen family ([Ar] $4s^2 3d^{10} 4p^4$), is positioned directly below sulfur and above tellurium. Selenium was first discovered in 1817 by Swedish chemist J. J. Berzelius.[47] The crystalline allotropes of selenium include the thermodynamically stable hexagonal (trigonal) metallic gray phase composed of Se_n helical chains, and several metastable forms such as monoclinic (α, β, and γ, based on Se_8 rings), rhombohedral (Se_6 rings), orthorhombic (Se_7 rings), and cubic (α and β) allotropic forms.[47] The non-crystalline allotropes of selenium can appear red, black, or brown in color and exist in an amorphous and glassy state. The metastable allotropes of selenium can be transformed into a stable hexagonal (trigonal) form through thermal treatment or chemical reactions. While the amorphous, monoclinic, and other metastable forms generally exhibit insulating behaviour, the hexagonal phase demonstrates a p-type semiconducting behavior due to the ordered arrangement of Se chains, which facilitates electronic conduction. Pourbaix diagrams of the important Se-based materials, including ZnSe, are presented in the SI. These diagrams illustrate the thermodynamically stable phases and possible transformations of these species under specific pH and potential conditions.

Selenium displays multiple oxidation states (−2, 0, +4, and +6), corresponding to selenide, elemental Se, selenite, and selenate, respectively.[48,49] The relative stability of these species depends on the redox environment and electrolyte conditions. In neutral to alkaline environments, Se^{4+} is the dominant species, whereas Se^{6+} prevails under acidic conditions.[48,49] Se^{6+} dominates under high redox potentials, while Se^{4+} is the primary species at moderate redox potentials. The ability of selenium to reversibly interconvert between Se^0, selenide, selenite, and selenate enables multielectron conversion reactions that yield high theoretical capacities. Its semiconducting properties, especially in the hexagonal crystalline phase, promote efficient electronic conductivity. Moreover, selenium has a relatively high volumetric energy density compared to sulfur, which makes it particularly suitable for compact, high-

Table 2 Comparative progress on Se cathodes for zinc ion batteries

Cathode	Anode	Electrolyte	Potential window (V)	Specific capacity	Capacity retention	Reference
Se/CMK-3 composite	Zn foil	1 M ZnTFSI in ethyl methyl carbonate (EMC)	0.05 to 2.2	551 mA h g_{Se}^{-1} at 0.1 A g^{-1}	81.2% after 500 cycles at 1 A g^{-1}	51
Se/CMK-3 composite	Zn foil	2 M ZnTFSI in PEG/water electrolyte	0.05 to 2.2	611 mA h g_{Se}^{-1} at 0.1 A g^{-1}	80.3% after 1000 cycles at 1 A g^{-1}	
Se–SnSe@BIBCs	Sn@BIBCs	$ZnSO_4$	0.01 to 2.0	603 mA h g^{-1} at 0.1 A g^{-1}	88.6% after 800 cycles at 5 A g^{-1}	53
Se@Activated carbon	Zn foil	30 m $ZnCl_2$ + 0.1 m Et_4NBr + 10 wt% PEO	0.1 to 1.9	2077.6 mA h g_{Se}^{-1} at	~42.7% after 200 cycles at 0.5 A g_{Se}^{-1}	56
Se@C	Zn foil	0.5 M $CuSO_4$ + 0.5 M $ZnSO_4$	1.05 to 1.60	1263 mA h g_{Se}^{-1} at 0.5 Ag^{-1}	400 cycles at 2 A g^{-1}	57
α-$Ru_{0.14}Se$	Zn foil	3 M ZnTFS	0.2 to 1.8 V	721 mA h g^{-1}	88.12% after 800 cycles at 5 A g-1	59
Se@CuN_4O/Cu_{ACs}	Zn foil	3 M ZnTFS	0.1 to 1.6 V	643 mA h g^{-1} at 0.2 A g^{-1}	93% after 3000 cycles at 5 A g^{-1}	60
Se/CuN_3P_1@C	Zn foil	3 M ZnTFS	0.1 to 1.6	756 mA h g^{-1} at 0.2 A g^{-1}	82.3% after 4000 cycles at 5 A g^{-1}	64
Se-CTF	Zn foil	1 M $ZnSO_4$ in PEGDME : water (94 : 6) mixture	0.1 to 2.1	630 mA h g^{-1} at 0.05 A g^{-1}	~70% after 1000 cycles at 0.0750 A g^{-1}	67
Se-in $Cu[Co(CN)_6]$	Zn foil	4 m ZnTFS + 20% PEO	0.1 to 2.1	664.7 mA h g_{Se}^{-1} at 0.2 A g^{-1}	90.6% after 6000 cycles at 5 A g^{-1}	66
TP-Se	Zn foil	1 M ZnTFS in acetonitrile: water (85 : 15) mixture	0.5 to 2.1	317 mA h g^{-1} at 0.5 A g^{-1}	85.3% after 4300 cycles at 2 A g^{-1}	71
PDSe/CMK-3	Zinc foil	3 M ZnTFS in PEG/H_2O	0.01 to 2.0	621.4 mA h g_{PDSe}^{-1} at 0.1 A g^{-1}	96.7% after 12 000 cycles at 10 A g^{-1}	72
di-Ph-Se	Zinc foil	30 m $ZnCl_2$	0.05 to 2.0	441 mA h g^{-1} at 0.5 A g^{-1}	77.3% after 500 cycles at 3 A g^{-1}	73

energy battery systems. As a result, selenium has been explored as a cathode material in numerous battery systems, including lithium and sodium, among others, where its multielectron redox reactions offer improved energy and power densities.[50]

As a chalcogen, selenium exhibits one of the highest intrinsic electronic conductivities among nonmetals ($\sim 1 \times 10^{-3}$ S m^{-1}). When used as a cathode, it can theoretically deliver an exceptionally high theoretical capacity of 678 mA h g^{-1} with two-electron conversion ($Se^0 \leftrightarrow Se^{2-}$). This limit can, in principle, be extended to 1357 mA h g^{-1} (four-electron) and 2036 mA h g^{-1} (six-electron) transfers under multivalent redox conditions. Although the theoretical capacity of selenium (678 mA h g^{-1}) is lower than sulfur (1675 mA h g^{-1}), the corresponding energy density of selenium (2403 Wh kg^{-1}) remains comparable to that of sulfur (2736 Wh kg^{-1}). Collectively, these attributes underscore selenium's promise as a cathode for aqueous zinc-ion batteries (AZIBs). An overview of recent progress in the development of Se-based cathodes is provided in Table 2. The Zn–Se conversion reaction (2-electron involvement) typically proceeds *via*:

$$\text{Anode: } Zn \leftrightarrow Zn^{2+} + 2e^-$$

$$\text{Cathode: } Se + Zn^{2+} \cdot 2e^- \leftrightarrow ZnSe$$

Porous carbon structured cathodes

The first demonstration of Zn–Se battery was reported by Zhi *et al.*[51] using a mesoporous carbon host with Se (Se/CMK) and 1 M ZnTFSI electrolyte. It was reported that a conversion-type Zn–Se battery system exhibits compatibility with both organic and aqueous electrolytes. As shown in Fig. 3a, cyclic voltammetry (CV) revealed a cathodic peak at 0.86 V (for $Se^0 \rightarrow Se^{2-}$) and corresponding reverse anodic peaks at 1.35 and 1.99 V (for $Se^{2-} \rightarrow Se^0$) in organic electrolyte (EMC, AN, and DMSO) during cycling. The corresponding galvanostatic charge–discharge (GCD) profiles shown in Fig. 3b, revealed capacity values of 551 mA h g_{Se}^{-1} with capacity retention of 89.1% after 100 cycles at 0.1 A g^{-1} rate in the EMC-based electrolyte. The *ex situ* XRD analysis (Fig. 3c and d) confirmed the conversion mechanism, as shown in the second discharge at 0.05 V of Se/CMK electrode. The diffraction peaks of elemental Se at 23.6° (100), 29.61° (101), and 43.71° (111) faded and appeared as new peaks at 24.91° (002), 27.71° (111), 44.91° (220), and 53.61° (311), corresponding to Se → ZnSe conversion.[52] In aqueous electrolyte, the same Se ↔ ZnSe conversion reaction yielded a 611 mA h g_{Se}^{-1} capacity at 0.1 A g^{-1} rate with a capacity retention of 80.3% after 1000 cycles at 1 A g^{-1} rate. Overall, the battery exhibited low voltage plateau slopes (0.94 V (A^{-1} h^{-1} g^{-1}) for organic and 0.61 V (A^{-1} h^{-1} g^{-1}) for aqueous systems due to its advanced conversion mechanism, enabling high energy densities up to 581 Wh kg Se^{-1} (organic) and 751 Wh kg Se^{-1} (aqueous), respectively.

Chen *et al.*[53] further advanced this concept using a bowl-in-ball structured carbon (BIBCs) material (Fig. 4a) that served as a nanoreactor, promoting the growth of tin-based materials. This approach enabled tackling sluggish reaction kinetics of Se cathodes, as well as mitigating dendrite growth issues on the zinc anodes.[53] The resulting Se–SnSe@BIBCs cathode exhibited a six-electron transfer (Se^{2-}/Se^{4+}) mechanism, delivering a limited capacity of only 614.8 mA h g^{-1} at a 0.1 A g^{-1} current rate, comparable to a two-electron process under similar conditions. Meanwhile, the Sn@BIBCs anode provided a well-distributed electric field strength, which promoted excellent reversibility of the zinc deposition/stripping process, facilitating uniform Zn deposition.

Recently, multielectron transfer in halogen chemistry has significantly enhanced cathode performance by leveraging their

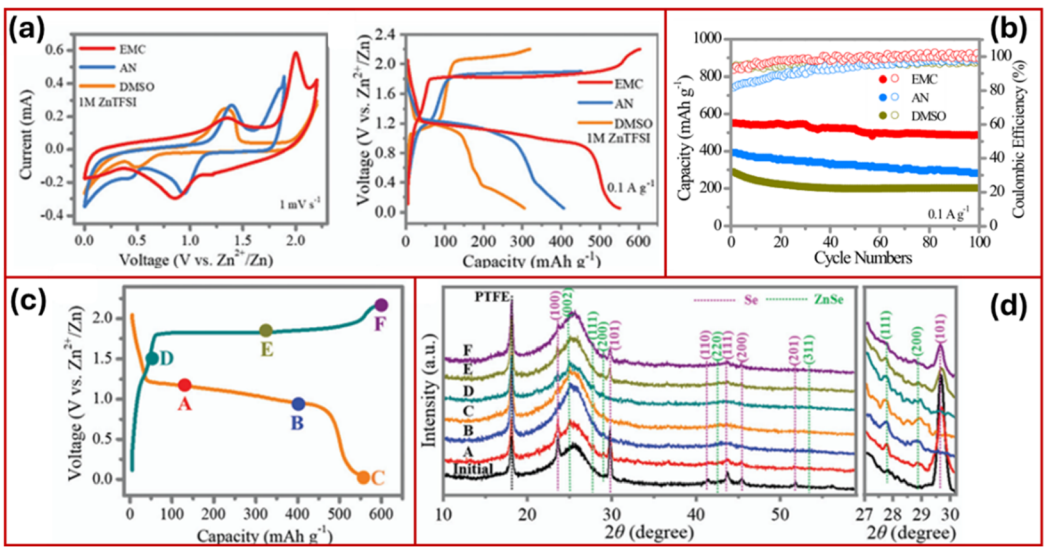

Fig. 3 Electrochemical performance of the Zn–Se battery with organic electrolytes. (a) CV curves at 1 mV s^{-1} and (b) GCD curves at 0.1 A g^{-1} based on 1 M ZnTFSI in EMC, AN, and DMSO at 1 mV s^{-1}, respectively. (c) GCD profile and (d) *ex situ* XRD patterns at selected potentials.[51] Reproduced from ref. 51 with permission from Royal Society of Chemistry, copyright, 2019.

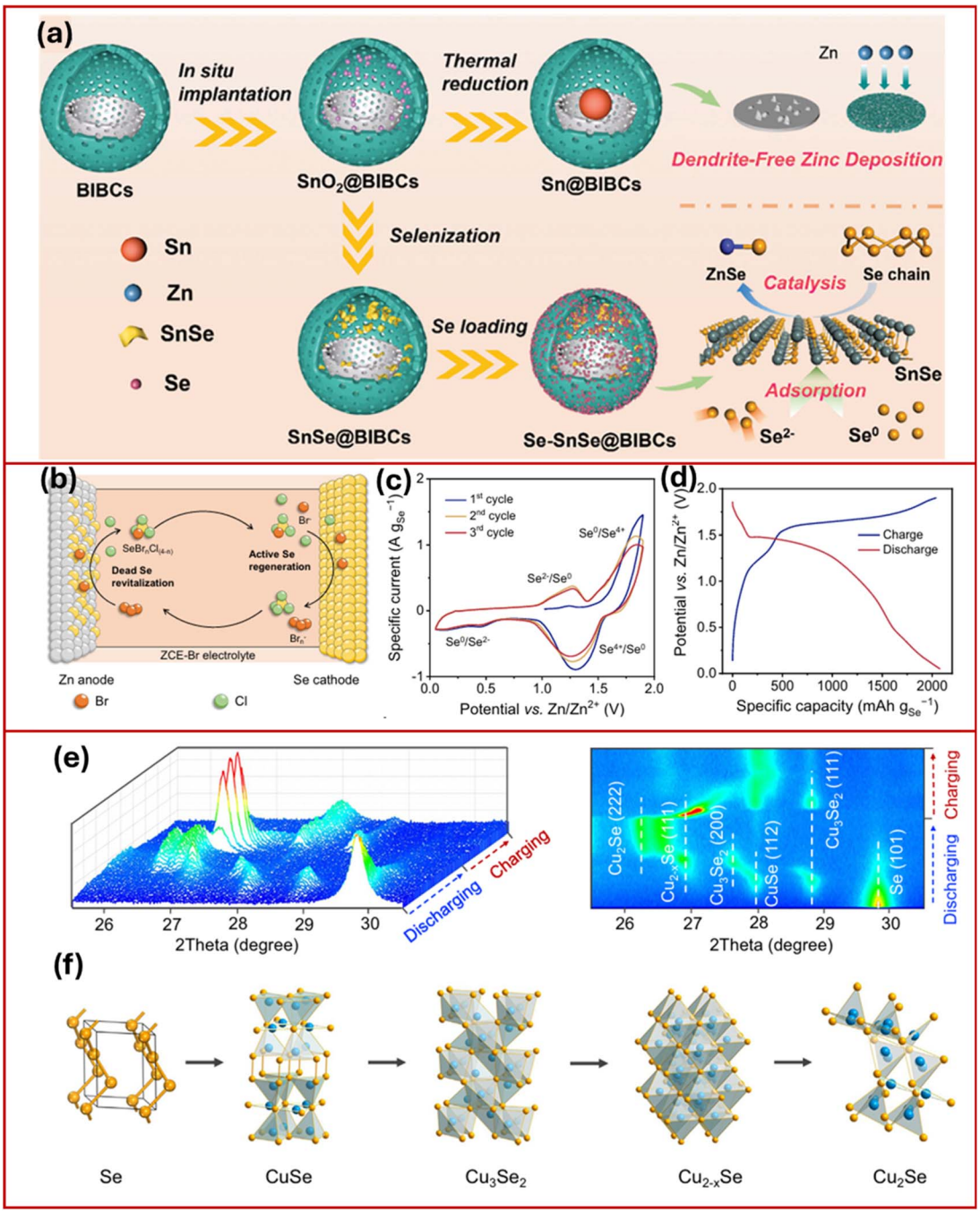

Fig. 4 Preparation process of (a) Sn@BIBCs, SnSe@BIBCs, and Se–SnSe@BIBCs.[53] Reproduced from ref. 53 with permission from Wiley-VCH, copyright 2024. (b) Zn–Se cell with ZCE-Br, (c) initial three-cycle CV curves at 0.1 mV s^{-1}, and (d) GCD profile at 0.5 A g_{Se}^{-1}.[56] Reproduced from ref. 56 with permission from Springer Nature, copyright 2025. Working mechanism investigations of a Se@C cathode with redox-active Cu^{2+} ions and a covalent triazine framework (CTF) cathode in AZIBs. (e) *In situ* XRD patterns to show the sequential conversion and (f) structure transition of Se during the discharge process in the Se@C cathode.[57] Reproduced from ref. 57 with permission from Springer Nature, copyright 2022.

unique electronic structure and exploiting a maximum number of valence electrons.[54,55] This approach has enabled achieving high energy density in zinc batteries with aqueous electrolytes. Yu *et al.*[56] developed a six-electron transfer redox process using ZnSe ↔ Se ↔ $SeCl_4$, enabled by the Br^-/Br_n^- redox couple (Fig. 4b). The conversion, initiated in a $ZnCl_2$-based hydrogel electrolyte, initially suffers rapid capacity decay due to the dissolution of $SeCl_4$ and its subsequent migration to the Zn anode, resulting in inactive ("dead") Se passivation. To address this issue, bromide salts were introduced as electrolyte additives, generating Br_n^- species that react with passivated Se on the Zn anode and regenerate active Se for cathodic reactions. This strategy enables reversible transitions between Se^{2-}/Se^0 and Se^0/Se^{4+} in a zinc-ion battery, delivering ultrahigh capacity of 2077.6 mA h g^{-1} as depicted in Fig. 4c and d. Despite this remarkable capacity, the battery suffered from limited cycling

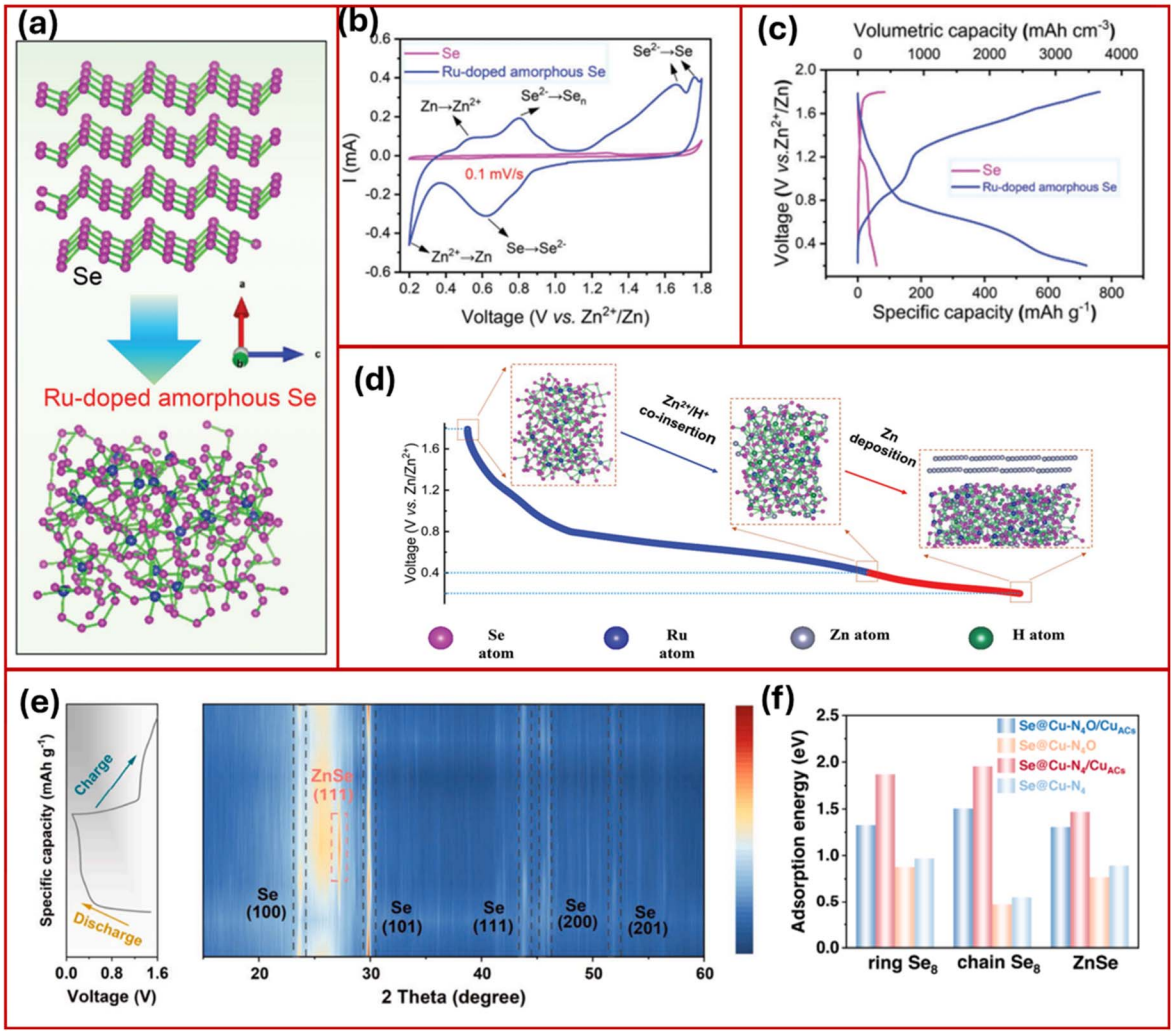

Fig. 5 (a) Schematic of structural transformation from crystalline Se to Ru-doped amorphous Se, (b) CV curves at 0.1 mV s^{-1} and (c) GCD profiles at 0.1 A g^{-1}, (d) schematic of storage mechanism of Ru-doped Se.[59] Reproduced from ref. 59 with permission from Wiley-VCH, copyright 2023. (e) Mechanism investigation using *ex situ* XRD and (f) adsorption energies calculated using DFT.[60] Reproduced from ref. 60 with permission from Elsevier, copyright 2025.

stability, underscoring the critical need for multifunctional catalytic host cathodes to stabilize multielectron redox processes and sustain long-term performance.

Qu *et al.*[57] reported an aqueous Se@C cathode employing redox-active Cu^{2+} ions as the charge carriers. This system enabled four-electron transfer through chronological conversion of Se ↔ CuSe ↔ Cu_3Se_2 ↔ $Cu_{2-x}Se$ ↔ Cu_2Se, lifting the theoretical gravimetric specific capacity to 1350 mA h g_{Se}^{-1}. Fig. 4e and f shows the *in situ* XRD pattern within the 25.5° to 30.5° range, confirming the four-electron involvement in the redox reaction and illustrating the structural transitions that occur during the cycling process. The corresponding Zn/Se full cell delivered a discharge voltage of 1.2 V and a capacity of 1263 mA h g_{Se}^{-1} at 0.5 Ag^{-1}.

Heteroatom doped cathodes

Heteroatom doping has also emerged as an effective approach to enhance the electrochemical performance of cathode materials. By modulating their electronic structure and surface chemistry, heteroatom dopants improve intrinsic conductivity, catalytic activity, and accelerate redox kinetics by lowering energy barriers, while introducing additional active sites for electrochemical reactions.[58] To address the limitations of conventional Se cathodes, Xu *et al.* reported a Ru-doped amorphous Se (Ru@Se) cathode that facilitated simultaneous proton and Zn^{2+} intercalation and delivered improved volumetric capacity and cycling stability.[59] Incorporating Ru into Se has proven to disrupt the Se–Se bonds in crystalline Se (Fig. 5a), leading to a rearrangement of Se atoms and the formation of a disordered atomic structure. This structural disorder narrowed the interlayer band gap, imparting metallic-like electrical conductivity and facilitating rapid charge transfer. As illustrated in Fig. 5b and c, cyclic voltammetry revealed the reversible Se ↔ Se^{2-} redox transition accompanied by co-intercalation of H^+/Zn^{2+} into the host and resulting in Zn^{2+} ↔ Zn^0 transition and delivering a high capacity of 721 mA h g^{-1}. *Ex situ* XRD measurement confirmed the formation of $Zn_x(CF_3SO_3)_y(OH)_{2x-y}$

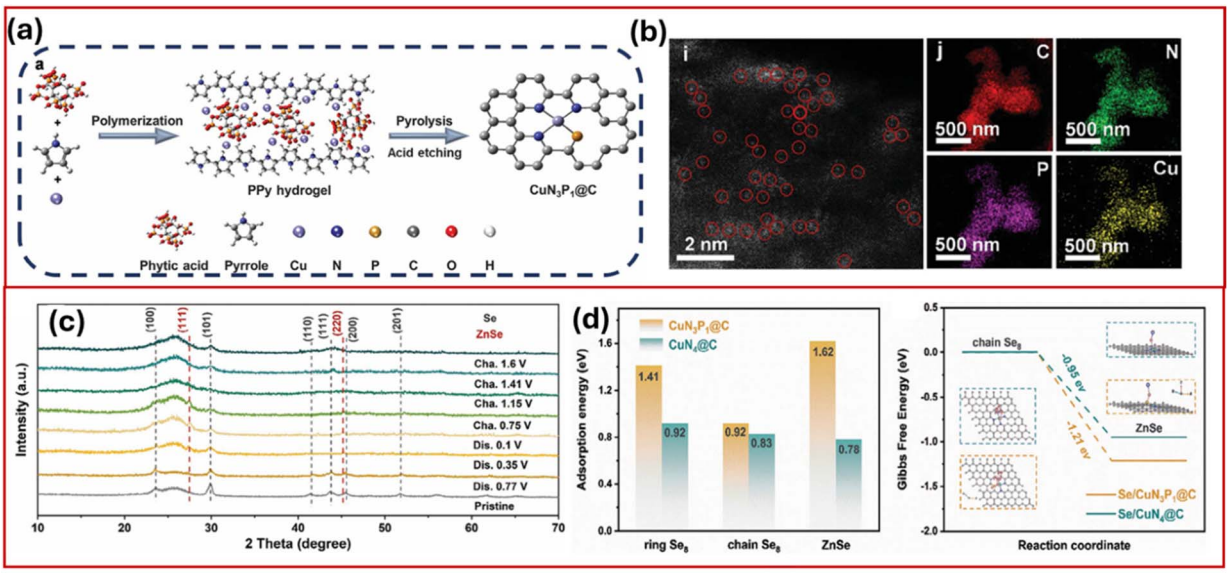

Fig. 6 (a) Synthesis process of and (b) enlarged EDS elemental mapping of CuN_3P_1@C, (c) *ex situ* XRD patterns, (d) adsorption energy of CuN_3P_1@C and CuN_4@C to ring Se_8, chain Se_8, and ZnSe, and Gibbs free energy.[64] Reproduced from ref. 64 with permission from Wiley-VCH, copyright 2025.

$\cdot nH_2O$ during discharge, providing indicative evidence of the H^+ insertion process. As depicted in Fig. 5d, the discharge process proceeds in two distinct stages. During the initial discharge stage (1.8–0.4 V), the α-$Ru_{0.14}Se$ cathode accommodates the co-insertion of Zn^{2+} and H^+ ions, which drives the reduction of elemental Se to Se^{2-}. In the subsequent low-voltage stage (0.4–0.2 V), the electrochemical process proceeds *via* a Zn plating reaction, wherein Zn^{2+} ions are reduced and deposited as metallic Zn within the cathode matrix. This dual-intercalation and plating mechanism effectively improves reaction reversibility and structural stability, marking a significant advancement in Se-based AZIB cathode design.

Single-atom catalysts (SACs) have emerged as a frontier strategy for engineering high-performance battery cathode design due to their unique electronic and structural characteristics.[61] Unlike conventional nanoparticle-based catalysts, SACs maximize metal atom utilization by anchoring isolated atoms onto a suitable substrate, thereby exposing every atom as an electrochemically active site.[61] The well-defined local coordination environment of single atoms enables precise modulation of the electronic structure, d-band center, and charge distribution, which collectively optimize adsorption energies of reaction intermediates and accelerate charge-transfer kinetics.[62] In battery cathodic processes, SACs can stabilize high-energy intermediates, suppress parasitic side reactions, and lower activation barriers, simultaneously improving capacity, rate capability, and long-term cycling stability.[63] These attributes make SACs a promising pathway toward next-generation Se-based cathodes that combine high energy density with exceptional durability. Liu *et al.*[60] developed a catalytic host comprising axially oxygen-coordinated Cu single atoms and neighboring Cu atomic clusters (CuN_4O/Cu_{ACs}) for a high-performance aqueous Zn–Se battery. Theoretical and experimental studies of CuN_4O/CuACs have revealed that adjacent CuACs can enhance the adsorption ability of the Cu active site for Se species, establishing an "adsorption balance effect" that stabilizes intermediate states during cycling. The energy storage mechanism was investigated using *ex situ* XRD (Fig. 5e), which revealed a pair of redox peaks attributed to the interconversion of Se ↔ ZnSe. Density functional theory (DFT) calculations (Fig. 5f) further demonstrated that the adsorption energies of chain-like Se and ZnSe on $Cu–N_4O/Cu_{ACs}$ are significantly lower than those on $Cu–N_4/Cu_{ACs}$. This reduction has been attributed to the modified electronic filling and the altered d-orbital energy levels induced by the presence of the axial O atom coordination. This optimized electronic configuration reduces reaction energy barriers and accelerates redox kinetics, enabling the $Cu–N_4O/Cu_{ACs}$ cathode to deliver a high specific capacity of 643 mA h g^{-1} with fast reaction kinetics.

In a subsequent study, Liu *et al.*[64] reported asymmetrically coordinated copper single-atom catalytic host material (Se/CuN_3P_1@C) using a melt-diffusion process that enabled efficient Se infusion into the host and significantly reduced the reaction energy barrier for the redox reaction between Se and Zn. As seen in Fig. 6a and b, CuN_3P_1@C was prepared using polypyrrole (PPy) hydrogel, and HAADF-STEM imaging confirmed uniformly dispersed Cu single-atom sites coordinated with N and P ligands. The higher phosphorus's electronegativity partially delocalizes Cu d-orbital electrons, lowering the d-band centre and enhancing directional adsorption of reactants (*e.g.*, Se^{2-}) and electron-transfer efficiency. The asymmetric N/P coordination breaks charge symmetry, creating polarized Cu sites that enhance directional reactant adsorption (*e.g.*, Se^{2-}) and electron transfer, while exposing undercoordinated Cu sites for catalytic activation. This cathode design boosted reaction kinetics and enabled ultrahigh battery

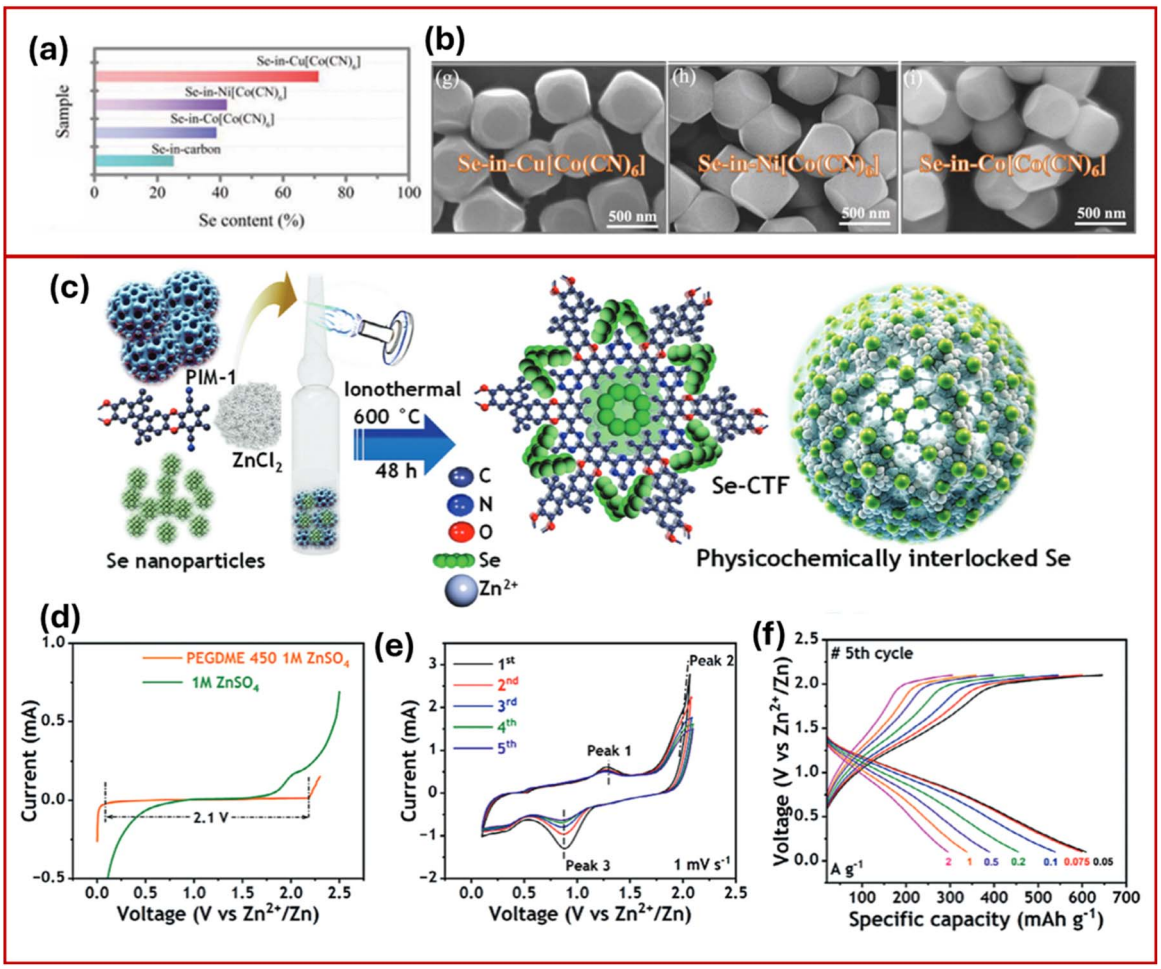

Fig. 7 (a) The Se content in porous carbon and (b) SEM images of PBA frameworks.[66] Reproduced from ref. 66 with permission from Wiley-VCH, copyright 2022. (c) Schematic depiction of Se-CTF cathode preparation, (d) LSV curves of 1 M $ZnSO_4$ in PEGDME 450, (e) CV curve of Se-CTF cathode at 1 mV s^{-1}, and (f) CD profile at different current rates.[67] Reproduced from ref. 67 with permission from Wiley-VCH, copyright 2024.

capacity. Owing to this, Se/CuN_3P_1@C achieved a high capacity of 756 mA h g^{-1} at 0.2 A g m^{-1} with a two-electron transfer process, confirmed by XRD patterns showing distinct peaks corresponding to alternating Se and ZnSe phases. The density functional theory (DFT) calculations (Fig. 6c and d) revealed that CuN_3P_1@C exhibits higher adsorption energies for ring Se_8 and lower reaction energy barrier for chain Se_8 to ZnSe conversion on CuN_3P_1@C (−1.21 eV) compared with CuN_4@C (−0.91 eV), highlighting the catalytic advantage of asymmetric coordination. This rational single-atom engineering strategy effectively accelerates interfacial redox kinetics and enhances selenium utilization, paving the way for next-generation high-rate, long-life Zn–Se batteries.

Conducting frameworks integrated cathodes

Increasing selenium loading in conventional carbon hosts typically results in poor utilization efficiency due to poor bulk conductivity, sluggish reaction kinetics, and structural degradation. To tackle these issues, selenium was embedded in other catalytic host materials like Prussian Blue Analogs (PBA), single-atom catalysts (*e.g.* CuN_3P_1@C), and SnSe. This approach has significantly improved selenium reaction kinetics and enhanced overall reversibility.[65] Additionally, the use of catalytic matrices can facilitate multielectron involvement and significantly increase the specific capacity per unit of selenium.

PBAs, characterized by their open three-dimensional frameworks and redox-active metal centres, provide efficient electron transport pathways and abundant active sites for catalytic reactions.[65] Zhi *et al.*[66] synthesized PBA-encapsulated Se cathodes ($Cu[Co(CN)_6]$@Se) using a coprecipitation method, achieving a high mass loading of Se (≈12.3 $mg_{(Se)}$ cm^{-2}) confined within the PBA framework. This approach effectively immobilized Se species enhanced the reaction kinetics and selenium utilization and mitigated the degradation issues commonly observed at high loadings. As shown in Fig. 7a and b, the synergetic integration between copper and cobalt species within the $Cu[Co(CN)_6]$ host effectively immobilized and catalysed a 6-electron conversion process (Se^{4+} ↔ Se^{2-}), with a remarkably low energy barrier (1.63 kJ mol^{-1}) and Tafel slope (95.23 mV dec^{-1}). As a result of this, the cathode delivered a high capacity of 664.7 mA h g^{-1} at 0.2 A g^{-1}, maintaining 430.6 mA h g^{-1} at 10 A g^{-1} and 90.6% capacity

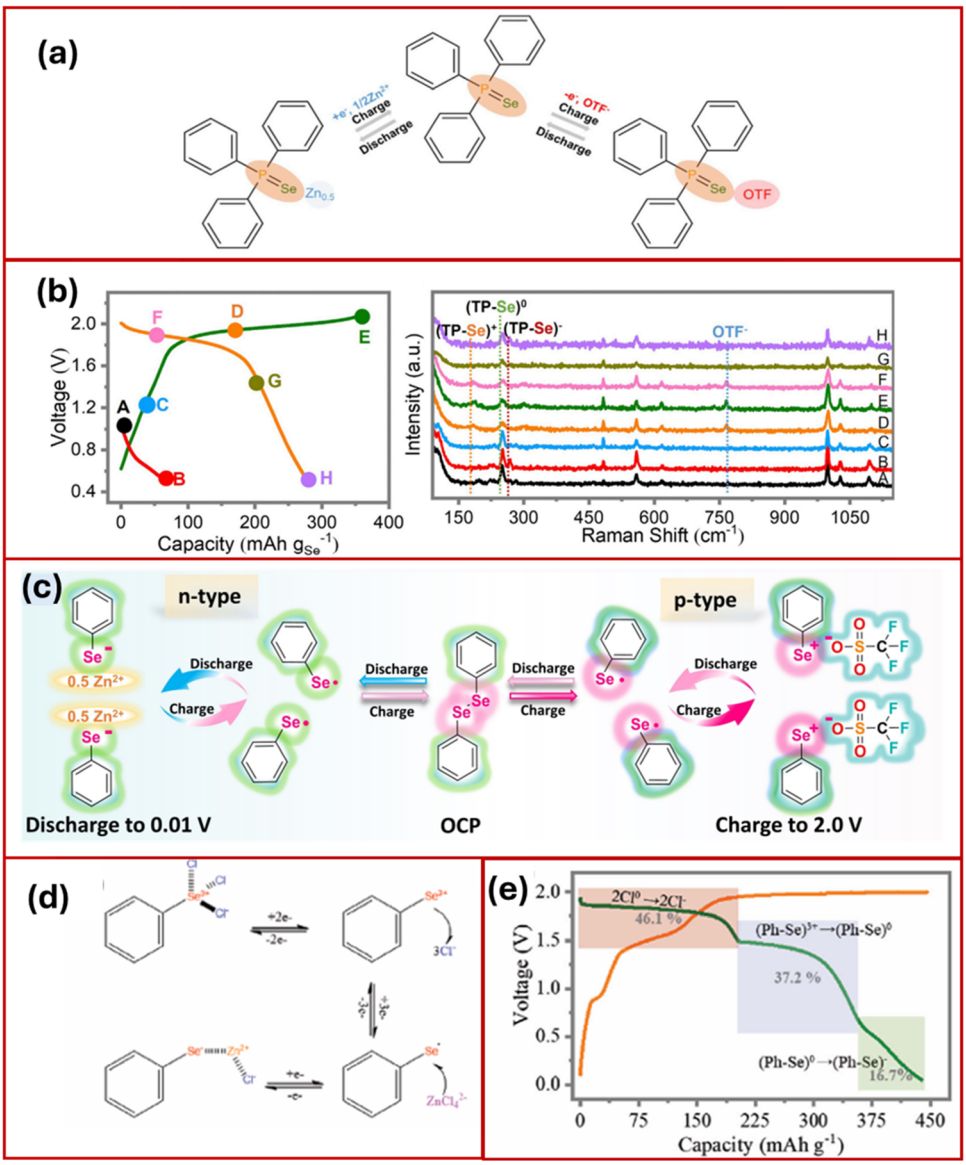

Fig. 8 (a) Structure changes and reaction mechanism of the ZnTP-Se battery, (b) GCD curves at 0.5 A g^{-1} with *ex situ* Raman patterns at selected potentials.[71] Reproduced from ref. 71 with permission from Cell Press, copyright 2022. (c) Structural changes in phenyl diselenide (PDSe) during cycling.[72] Reproduced from ref. 72 with permission from Wiley-VCH, copyright 2024. (d) Structural changes in diphenyl diselenide (di-Ph-Se) during charging and (e) GCD curves at 0.5 A g^{-1}.[73] Reproduced from ref. 73 with permission from Wiley-VCH, copyright 2023.

retention after 6000 cycles. *Ex situ* XPS analysis confirmed that the PBA facilitates multi-electron (6e$^-$) redox transitions from Se^0 to Se^{4+} and subsequently to Se^{2-}, validating the proposed catalytic mechanism.

Koratkar *et al.*[67] developed a highly conducting covalent triazine framework (CTF) host to physicochemically lock selenium (Se$_8$) clusters (Se-CTF), which enabled the suppression of the polyselenide shuttle effect and provided high specific capacity and cyclic stability in AZIBs. As schematically represented in Fig. 7c, the Se-CTF was synthesized by infiltrating Se into the polymers of intrinsic microporosity (PIM-1) precursor, followed by a one-step ionothermal process, resulting in Se clusters interlocked within the CTF matrix. For the electrolyte, they opted for a molecular crowding agent, polyethylene glycol dimethyl ether (PEGDME 450), a solvent with anodic stability up to ~2.1 V (Fig. 7d) that enables suppression of water activity despite a low zinc concentration (1 M $ZnSO_4$). The CV profiles (Fig. 7e and f) revealed a typical Se^0 ↔ Se^{2-} redox conversion. The Se-CTF cathode delivered a capacity of ~600 mA h g^{-1} at ~0.075 A g^{-1} with about 70% retention after 1000 cycles.

Organic cathodes

Beyond conventional inorganic Se cathodes, organic cathode materials have emerged as promising candidates for high-performance Zn–Se chemistry due to their tunable molecular structures.[31,68] Incorporation of O, S, or Se atoms into organic Se-based molecules through coordination with strong electron-withdrawing groups or conjugated structures can effectively reduce the surface charge density of these chalcogen elements.

Such modulation can be achieved through rational molecular design.[69] Moreover, in the presence of suitable anions acting as strong nucleophiles, a positive valence conversion of chalcogen-based functional groups can be realized, thereby expanding the redox versatility of these materials.[70] Zhi *et al.*[71] demonstrated this concept using organoselenium compound triphenylphosphine selenide (TP-Se) as a cathode for the Zn–Se battery system. As depicted in Fig. 8a and b, the TP-Se cathode displays a dual ion conversion mechanism from $(TP\text{-}Se)^-$ to $(TP\text{-}Se)^0$ and then to $(TP\text{-}Se)^+$ facilitated by Zn^{2+}/triflate (OTF^-) ions, indicating both n- and p-type processes in the cathode. The reaction mechanism can be described as follows:

$$\text{Anode: } Zn^{2+} + 2e^- \leftrightarrow Zn$$

$$\text{Cathode: } Zn_{0.5}\text{TP-Se} \leftrightarrow \text{TP-Se} + \tfrac{1}{2}\,Zn^{2+} + e^- \text{ (first step)}$$

$$\text{TP-Se} + OTF^- \leftrightarrow \text{TP-Se-OTF} + e^- \text{ (second step)}$$

This dual-ion Zn-TP-Se battery exhibited a flat discharge plateau at 1.96 V, excellent discharge capacity, and outstanding cycling performance, lasting up to 4300 cycles.

Li *et al.*[72] reported bipolar organic cathode materials (OCMs) with phenyl diselenide (PhSe-SePh, PDSe), which feature active Se active sites capable of dual-ion storage. In this cathode material, Se atoms are bonded to conjugated groups that can undergo multi-electron redox processes, involving both positive-valence oxidation and negative-valence reduction, thereby enabling higher redox potentials and improved reversible capacities. As depicted in Fig. 8c, the PDSe follows a sequential conversion reaction mechanism: $(PhSe)^- \leftrightarrow (PhSe\text{-}SePh)^0 \leftrightarrow PhSe$. During cycling, diselenide bonds are regularly broken and rebuilt with dynamically coordinating with Zn^{2+} and OTF^- ions. When integrated with ordered mesoporous carbon (CMK-3), the PDSe-based cathodes attained high reversibility capacity (621.4 mA h g^{-1}), high energy density (578.3 Wh kg^{-1}), and extended lifespans (over 12 000 cycles) at high discharge rates.

Halogen redox reactions, such as the chlorine redox reaction (ClRR), offer high potential for high-energy storage applications due to their high voltage and capacity. However, practical deployment remains challenging due to issues such as Cl_2 leakage, which severely compromises battery efficiency and stability. Zhi *et al.*[73] introduced diphenyl diselenide (di-Ph-Se) as Se-based anchoring agent, stabilizing Cl at the atomic level through chalcogen-halogenocordinating chemistry. The charge storage capacity of the cathodes involved three sequential conversion processes (Fig. 8d and e), delivering 203 mA h g^{-1} ($Cl^{0/-}$), 164 mA h g^{-1} ($(Ph\text{-}Se)^{3+/0}$), and 74 mA h g^{-1} ($(Ph\text{-}Se)^{0/-}$), with 46.1%, 37.2%, and 16.7% contribution, respectively. The overall storage reaction is described as:

$$Ph\text{-}SeZnCl + 2\,ZnCl_4^{2-} \leftrightarrow (Ph\text{-}SeCl_3)^{2+} + 6Cl^- + 3Zn$$

This conversion reaction enables a six-electron conversion process, resulting in a high discharge capacity of 507 mA h g^{-1}, an average voltage of 1.51 V, and an energy density of 665 Wh kg^{-1}, while demonstrating suppressed self-discharge. These results highlight the effectiveness of Se-based anchoring strategies in enabling reversible and efficient halogen redox chemistry for advanced battery systems.

Electrolyte modification strategies for Zn–Se batteries

In AZIBs, electrolyte engineering has attracted increasing attention in recent years, as tailoring the electrolyte composition enables control over the electrochemical properties, anode–electrolyte interface, and electrochemical and chemical stability of the cathode.[74] The aqueous electrolyte plays a crucial role in facilitating the fast diffusion of Zn^{2+} between the Zn anode and the Se/Te cathode, thereby governing the reaction mechanism. Moreover, electrolyte modification can also tune redox potentials and help suppress parasitic side reactions. Primarily, $ZnSO_4$ and ZnTFS aqueous solutions have been widely used because they offer a broad electrochemical stability window (ESW) and good electrode compatibility.[75] In particular, ZnTFS enhances overall battery performance because its TFS^- anions can suppress HER and dendrite formation. It also promotes the formation of stable, protective layers on the zinc metal anode, thereby enhancing cycling stability. Consequently, early reports of Zn–Se batteries using ZnTFS electrolytes demonstrated high capacity and long-term stability.[59,60,64]

Employing organic solvents as co-solvents in aqueous electrolytes can also reduce water activity and improve cathode stability. Koratkar *et al.* reported a cost-effective molecular crowding agent (PEGDME 450) as a cosolvent (94% PEGDME 450 + 6% DI water with 1 M $ZnSO_4$) for suppressing water splitting and widening the ESW of the aqueous electrolyte.[67] As shown in Fig. 7d, in the absence of PEGDME, the water splitting of 1 M $ZnSO_4$ aqueous electrolyte started at ~1.8 V. However, upon addition of the crowding agent at the same salt concentration, the onset voltage shifted to ~2.1 V, pushing the reaction potentials well beyond the thermodynamic stability of water. As a result, the Zn–Se cell with a Se-CTF cathode featuring a selenium locking mechanism exhibited long-term capacity retention over 1000 cycles. The report from Zhi *et al.* using 1 M ZnTFS in acetonitrile–water (85 : 15) mixture also extended the ESW up to 2.29 V *vs.* Zn^{2+}/Zn and enhanced the capacity.[71] Using high-concentration, salt-rich electrolytes (SRE) is another effective method to promote dendrite-free Zn deposition, suppress HER, and extend the ESW.[76] With a 30 m $ZnCl_2$ electrolyte (ZCE), Yu *et al.* enabled Se^0/Se^{4+} conversion kinetics with reduced water reactivity. However, the dead-Se formation limited long-term performance. This issue was resolved by adding 0.1 m Et_4NBr (ZCE-Br) as an additive, which revitalized dead Se and significantly improved the capacitive response (2077.6 mA h g_{Se}^{-1}) and cycling stability.[56] Zhi *et al.* employed a 30 m $ZnCl_2$ electrolyte in which $ZnCl_4^{2-}$ was the dominant anionic species, effectively suppressing water activity to eliminate oxygen evolution reactions and ensuring sufficient Cl^- availability during charge–discharge cycling.[73] Notably, a six-electron transfer process occurred during charge–discharge in the di-Ph-Se cathode with four electrons from the conversion between $(Ph\text{-}Se)^-$ and $(Ph\text{-}Se)^{3+}$ and two electrons from the

conversion between Cl^- and Cl^0. Polymer additives have also been explored, offering improved ionic conductivity, suppressed dendrite growth, and enhanced mechanical stability, leading to longer cycle life. A gel electrolyte consisting of 20% PEO and 4 m ZnTFS exhibited high ionic conductivity and an extended ESW of 2.64 V.[66] Li *et al.* reported a series of polyethylene glycol (PEG)-ZnTFS mixtures (0, 25, 50, 75, and 100 vol%) with excellent non-flammability for phenyl diselenide cathodes.[72] Among them, 25 vol% PEG provided good fluidity, a decent ESW, and safe operation at high temperature, outperforming conventional organic solvent electrolytes.[72]

Tellurium (Te) cathodes for zinc-ion batteries

Tellurium (Te), discovered by Müller in 1782, is a chalcogen element located below sulfur and tellurium in the periodic table. Te exhibits multiple crystallographic allotropes, with the hexagonal phase being the thermodynamically most stable form under ambient conditions. Along with hexagonal form, Te also exists in other metastable crystalline phases, including monoclinic, orthorhombic, and cubic (α- and β-) phases, which are generally obtained under special synthetic conditions and tend to revert to stable hexagonal phase upon heating or prolonged storage.[77] Pourbaix diagrams for key telluride-based materials, including ZnTe, are included in the SI. These diagrams illustrate the potential chemical changes these materials may undergo across different pH levels and electrochemical potentials.

The intrinsic properties of Te make it a promising electrode material for rechargeable batteries. Te possesses high electrical conductivity ($\sim 2 \times 10^2$ S m^{-1}), approximately 30 order of magnitude higher than that of sulfur, enabling superior electrochemical activity and faster kinetics during cycling. Tellurium, owing to its high density (6.24 g cm^{-3}), can deliver a remarkable theoretical volumetric capacity of 2621 mA h cm^{-3}, which is comparable to sulfur (3467 mA h cm^{-3}) and selenium (3254 mA h cm^{-3}). However, its gravimetric capacity remains relatively modest at 420 mA h g^{-1}.[78] An overview of recent advances in the development of Te-based cathodes is presented in Table 3.

3D architectures of Te cathodes

The first ever Zn–Te battery was reported by Zhi *et al.*[79] using tellurium nano sheets (Te NSs) as a cathode. The battery delivered ultrahigh volumetric capacity of 2619 mA h cm^{-3} in galvanostatic cycling with potential limitation (GCPL), as depicted in Fig. 9a. The Zn–Te battery operates *via* conversion reaction, demonstrating a two-step solid-to-solid conversion of tellurium (Te) to zinc ditelluride ($ZnTe_2$) and then to zinc telluride (ZnTe), as confirmed by *ex situ* XRD and XPS analyses. The battery operates through a two-step conversion:

$$\text{First step: } 2Te + Zn^{2+} + 2e^- \leftrightarrow ZnTe_2$$

$$\text{Second step: } ZnTe_2 + 2e^- \leftrightarrow 2ZnTe$$

Table 3 Summary of the performance of Te cathodes in Zn–Te batteries

Cathode	Anode	Electrolyte	Potential window (V)	Specific capacity	Capacity retention and cyclic stability	Reference
Te nanosheets (Te NSs)	Zn foil	1 M $ZnSO_4$	0.2 to 1.7	419 mA h g^{-1} at 0.05 A g^{-1}	82.8% after 500 cycles at 1 A g^{-1}	79
Te HNTs	Zn foil	1 M $ZnSO_4$	0.2–1.7 V	376.56 mA h g^{-1} at 50 mA g^{-1}	90.42% after 100 cycles at 500 mA g^{-1}	80
Te	Zn foil	1 M $ZnSO_4$	0.20–1.55 V	460 mA h g^{-1} at 50 mA g^{-1}	N. A.	81
Nano-Te	Zn foil	2 M $ZnSO_4$ + 0.025 M $ZnCl_2$ + 2 vol% acetonitrile + 0.05 M glucose	0.2–1.35 V	2409 mA h cm^{-3} at 0.2 A g^{-1}	N.A. Stability upto 5000 cycles at 4 A g^{-1}	82
n-TeO_2/C	Zn foil	2 M $ZnSO_4$	0.1–1.6 V	955 mA h g^{-1} at 0.1 A g− 1	N.A. Stability upto 200 cycles at 2 A g^{-1}	83
Te-rGO	Zn foil	2 M $ZnSO_4$	0.2–1.6 V	621 mA h g^{-1} at 0.05 A g^{-1}	N.A. upto 2500 cycles at 6 A g^{-1}	84
Te-graphite	Zn foil	30 M $ZnCl_2$	0.1–1.9 V	1223.5 mA h g_{Te}^{-1} at 0.4 A g^{-1}	65% after 300 cycles at 1.5 A g_{Te}^{-1}	85
Te@CSs	Zn foil	BMIMCl + EG 30 $ZnCl_2$ (1 : 0.3 : 1.2)	0.1–1.8 V	802.7 mA h g^{-1} at 0.1 A g^{-1}	81.3% after 400 cycles at 1 A g^{-1}	86
Te–MoS_2@NFC	Zn foil	3 M ZnTFS	0.1–1.8 V	483 mA h g^{-1} at 150 mA g^{-1}	84% after 1200 cycles at 1500 mA g^{-1}	87
Te/MnO@NC	Zn foil	3 M ZnTFS	0.1–1.8 V	429 mA h g^{-1} at 0.1 A g^{-1}	N.A. 2500 cycles at 3 A g^{-1}	88
Te–MoO_2/NC	Zn foil	3 M ZnTFS	0.1–1.8 V	493 mA h g^{-1} at 0.1 A g^{-1}	N.A. 4000 cycles at 2 A g^{-1}	89
Te/$MoSe_2$@ rGO	Zn foil	3 M ZnTFS	0.1–1.8 V	450 mA h g^{-1} at 0.15 A g^{-1}	92% after 1100 cycles at 2 A g^{-1}	90
$NiTe_2$ nanosheets	Zinc foil	1 M $ZnSO_4$	0.2–1.8 V	510 mA h g^{-1} at 50 mA g^{-1}	97.2% after 400 cycles at 2000 mA g^{-1}	91
Te/$CH_3NH_3PbI_3$/TiO_2	Zinc foil	3 M $ZnSO_4$	0.3–1.5 V	720 mA h g^{-1} at 100 mA g^{-1}	N. A. 10 cycles at 100 mA g^{-1}	92

The initial conversion step displays a flat plateau, providing a stable output potential. Galvanostatic intermittent titration technique (GITT) investigation confirmed that nearly 74.1% of the total capacity originates from the first-step conversion reaction. This battery system excels in capacity retention, demonstrating over 82.8% retention after 500 cycles, largely due to the elimination of the "shuttle effect" associated with solid-to-solid transitions.

Yu *et al.*[80] reported hexagonal-shaped tellurium nanotubes (Te HNTs) with an average length of 5–6 μm and a diameter of 0.2–0.3 μm (Fig. 9c). Single-crystalline structure was confirmed in the nanotubes, showing lattice spacings of 0.387 nm for the (100) planes and 0.587 nm for the (001) planes, indicating growth along the (001) direction (Fig. 9d). First-principles calculations suggested that this single-crystalline nature and growth orientation facilitate zinc ion migration. The hollow interior of Te HNTs enabled the alleviation of volume changes during charge and discharge cycles. The material exhibited high electrical conductivity and good compatibility with aqueous electrolytes, leading to high battery performance with capacities of 387.73 and 223.25 mA h g^{-1} at 50 and 2000 mA g^{-1}, respectively (Fig. 9e). The Te HNTs also delivered an improved capacity retention of 90.42% after 100 cycles at 500 mA g^{-1}, outperforming conventional Te powder electrodes.

Cui *et al.*[81] proposed a sequential conversion reaction involving H^+ and Zn^{2+} in aqueous Zn/Te chemistry, enabling a six-electron transfer and achieving notable capacity exceeding 460 mA h g^{-1} at a discharge rate of 50 mA g^{-1}.[81] They proposed cathodic conversion processes are as follows:

$$H_2O \leftrightarrow H + OH^-$$

$$TeO_2 + 4H^+ + 4e^- \leftrightarrow Te + 2H_2O$$

$$Te + Zn^{2+} + 2e^- \leftrightarrow ZnTe$$

$$3Zn^{2+} + 6OH^- + ZnSO_4 + 4H_2O \leftrightarrow Zn_4SO_4(OH)_6 \cdot 4H_2O$$

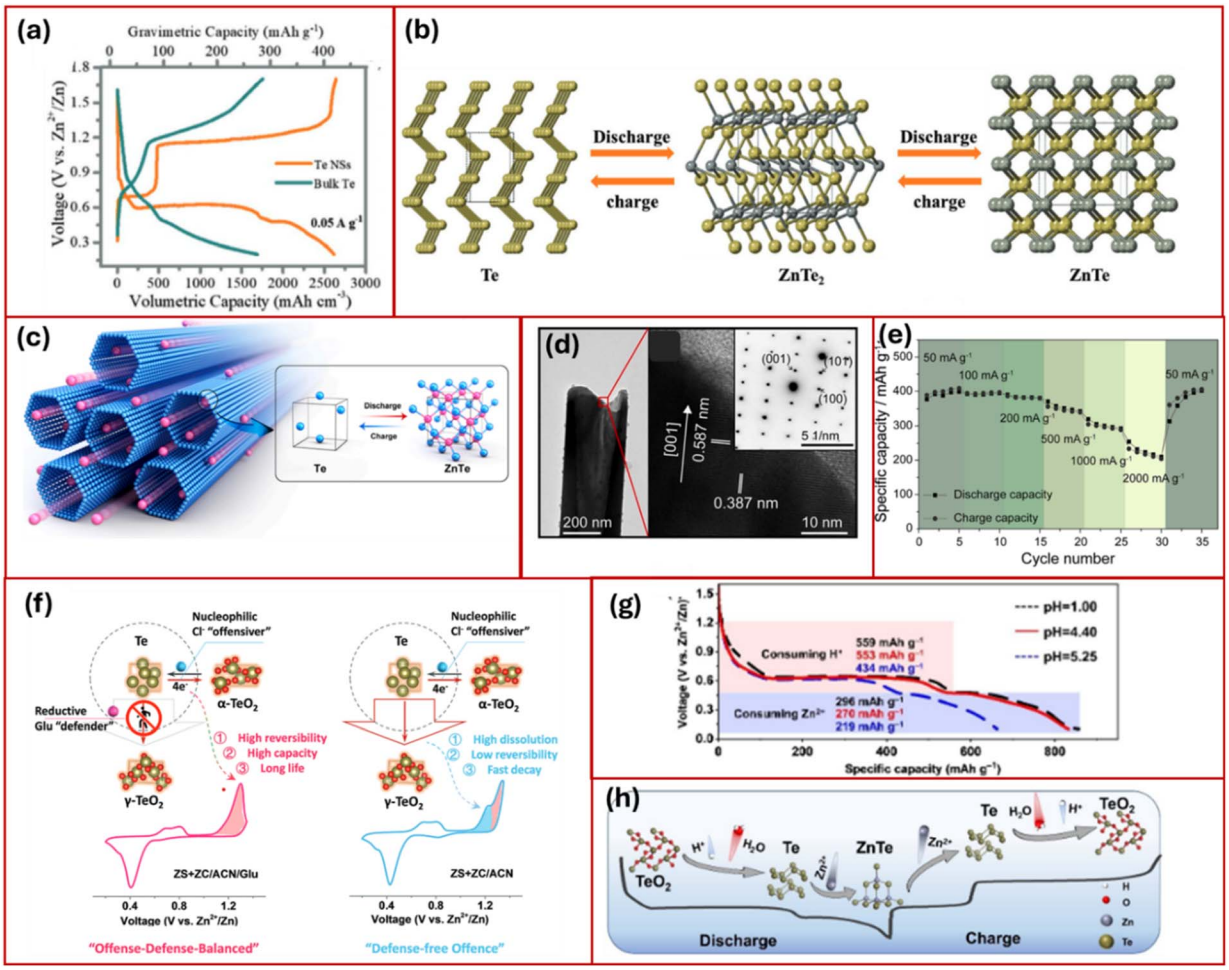

Fig. 9 (a) GCPL curves of Te NSs and bulk Te at 0.05 A g^{-1} and (b) schematic representation for phase transformation during discharging.[79] Reproduced from ref. 79 with permission from Wiley-VCH, copyright 2020. (c) Representation of zinc ion diffusion, (d) TEM images showing one end of a Te HNTs and (e) rate capability at different current density.[80] Reproduced from ref. 80 with permission from Elsevier, copyright 2023. (f) Illustration of offense–defense reaction pathways.[82] Reproduced from ref. 82 with permission from Wiley-VCH, copyright 2023. (g) CD curves of n-TeO_2/C in 2 M $ZnSO_4$ with different pH, and (h) schematic design of six electron transfer.[83] Reproduced from ref. 83 with permission from Wiley-VCH, copyright 2023.

Overall, the charge storage mechanism involves the transformation between TeO_2 and Te, and the subsequent conversion of Te to ZnTe. *Ex situ* XRD studies confirmed this mechanism, highlighting a novel reaction pathway for high-performance aqueous zinc–tellurium batteries.

In 2023, Li *et al.* developed an offense–defense–balanced strategy (Fig. 9f) to enhance Te^0/Te^{4+} conversion in aqueous zinc batteries. By co-introducing nucleophilic chlorine ions (Cl^-) and reductive glucose (Glu), this approach addresses significant issues of poor kinetics and capacity decay.[82] The Cl^-/Glu co-additive effectively retained the nucleophilic promotion effect of Cl^- on the Te^0/Te^{4+} conversion and suppressed the formation of the Cl^--induced metastable γ-TeO_2 phase, thereby enabling a deeper and more reversible Te^0/Te^{4+} redox process. This unique co-additive approach lowered the activation energy for Te conversion from 61.4 to 52.8 kJ mol^{-1} and delivered capacity close to theoretical values with an extended lifespan.

Carbon composite Te cathodes

Another six-electron transfer mechanism using nano-sized TeO_2/C (n-TeO_2/C) cathode was reported by Zhu's group.[83] The integrated nanostructure and carbon matrix facilitated efficient zinc-ion transport, enabling $TeO_2 \leftrightarrow Te$ and $Te \leftrightarrow ZnTe$ conversions. The n-TeO_2/C cathode achieved a high discharge capacity of 955 mA h g^{-1} at 0.1 A g^{-1}, corresponding to 94.7% of the theoretical six-electron capacity. With proton participation, the six-electron transfer of TeO_2 proceeds through a three-phase conversion in acidic electrolytes. Comparative studies in different electrolyte environments (Fig. 9g and h) confirm that this reversible six-electron reaction is proton-dependent, revealing a mechanism in which protons are generated during charging and consumed during discharging, establishing the operational mechanism for the n-TeO_2/C composite in AZBs.[81]

To date, Te cathodes have been limited by sluggish conversion kinetics, pronounced volume expansion/contraction during cycling, mechanical degradation, loss of electrical contact, and limited cycling stability.[93] To mitigate these challenges, highly catalytic active porous carbon host materials have been employed to uplift the electrochemical performance. Li's group reported hierarchical Te-reduced graphene oxide (Te-rGO) structure where Te nanorods wrapped firmly in low percentage graphene to mitigate large volume expansion.[84] The strong affinity of chemical Te–C bonds between Te and graphene improved conductivity and structural stability, accommodating over 90% Te content. As a result, the 1D Te nanorods promoted axial charge transport and maximized the usage of active material, demonstrating a two-step solid conversion mechanism of Te to $ZnTe_2$ to ZnTe during cycling.

The reaction mechanism of Zn–Te batteries is inherently complex due to the intricate, multi-step conversion processes and the effects of electrolyte acidity, which complicate the identification of intermediates. However, recent efforts have focused on introducing nucleophilic chloride ions into the electrolyte to enable Te^0/Te^{4+} conversion, which accounts for nearly two-thirds of the total capacity.[80] Zhi and his group reported a stepwise, reversible $Te^{2-} \leftrightarrow Te^0 \leftrightarrow Te^{2+} \leftrightarrow Te^{4+}$ redox conversion pathway involving six electron transfers using a microporous carbon sphere-encapsulated Te (Te@CSs) cathode in a highly concentrated $ZnCl_2$ electrolyte.[80] The Cl^- ions act as strong nucleophiles, stabilizing Te^{n+} ions intermediates and facilitating multivalent conversion in Te cathodes as follows:[82,86]

$$\text{Step 1. } ZnTe + 4Cl^- \leftrightarrow Te + ZnCl_4^{2-} + e^-$$

$$\text{Step 2. } Te + Cl^- \leftrightarrow TeCl^+ + 2e^-$$

$$\text{Step 3. } TeCl^+ + 2Cl^- \leftrightarrow TeCl_3^+ + 2e^-$$

$$\text{Overall reaction: } ZnTe + 2ZnCl_4^{2-} \leftrightarrow TeCl_3^+ + 5Cl^- + 3Zn$$

As depicted in Fig. 10a, this system exhibits three distinct discharge plateaus at 1.24, 0.77, and 0.51 V, corresponding to capacities of 30.4%, 36.7%, and 32.9%, respectively, and a total capacity of 802.7 mA h g^{-1}. In each conversion step, there is equal electron transfer. To further stabilize the Te^{n+} intermediates, modified ionic liquid (IL) electrolytes have been employed, resulting in a high areal capacity of 7.13 mA h cm^{-2}, excellent cycling stability, and a low self-discharge rate.

In a related strategy, a Te-graphite cathode (TeG) in a 30 m $ZnCl_2$ electrolyte enables a six-electron redox-amphoteric conversion by breaking hydrogen bonding in the water structure, limiting the water reactivity to Te^{4+} hydrolysis.[85] The highly concentrated $ZnCl_2$ electrolytes yielded high solubility and stability for $TeCl_4$ species (Fig. 10c), thereby limiting Te hydrolysis. *Operando* synchrotron X-ray absorption spectroscopy provided comprehensive evidence of six electron transfer with $Te^{2-}/Te^0/Te^{4+}$ conversion, with $TeCl_4$ identified as the fully charged product and ZnTe as the fully discharged product.

Heterostructure engineered Te cathodes

The use of metallic Te as a cathode in ZIBs is often limited by poor electrochemical conversion and significant volume fluctuations, resulting in a limited cycling life. To resolve these challenges, Liu and his group have explored other catalytically active matrices beyond conventional carbon materials to host Te. The materials included MoO_2/NC, MnO@NC, $MoSe_2$@rGO, and MoS_2@NFC, which were used as catalysts for two-electron conversion in the Te cathode.[87–90] Liu *et al.* reported *in situ* growing MoS_2 on N, F co-doped porous carbon nanosheets (MoS_2@NFC) hierarchical structure hosting Te.[87] High-resolution TEM images Fig. 10d reveal the catalytic matrix, which significantly accelerates the Te redox kinetics. As a result, the aqueous Zn–Te battery with $Te \leftrightarrow ZnTe$ conversion mechanism delivered a high capacity of 483 mA h g^{-1} at 150 mA g^{-1} (Fig. 10e), along with excellent rate performance and cycling stability.

Another report from the same group reported manganese oxide (MnO) hollow nanospheres loaded on nitrogen-doped carbon nanosheets as a host for Te in a Zn–Te battery cathode (Te/MnO@NC).[88] The integration of MnO@NC facilitated

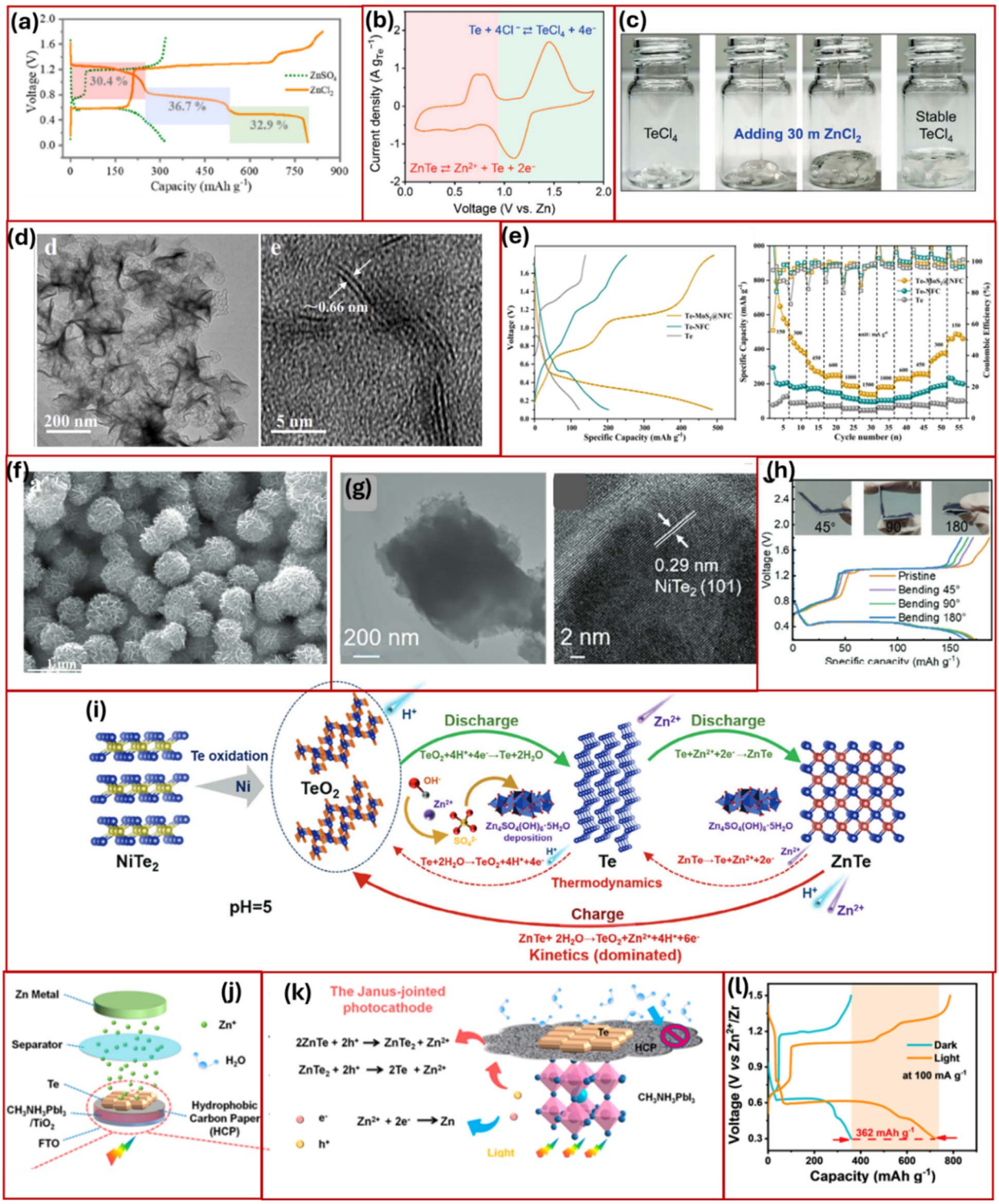

Fig. 10 (a) GCD curves of Te-based electrodes with different electrolytes at 0.1 A g^{-1}.[86] Reproduced from ref. 86 with permission from American Chemical Society, copyright 2023. (b) CV curve of TeG at 0.2 mV s^{-1}, (c) optical photos of 30 m $ZnCl_2$ with $TeCl_4$.[85] Reproduced from ref. 85 with permission from Wiley-VCH, copyright 2024. (d) HRTEM images, (e) GCD curves at 150 mA g^{-1} and rate capability of the MoS_2@NFC.[87] Reproduced from ref. 87 with permission from Elsevier, copyright 2023. (f) SEM image of MoO_2/NC.[89] Reproduced from ref. 89 with permission from Wiley-VCH, copyright 2023. (g) TEM and HRTEM image of $NiTe_2$ nanosheets, (h) GCD curves at different bending of pouch cell, (i) reaction mechanism plan of the electrolyte with pH 5.[91] Reproduced from ref. 91 with permission from Wiley-VCH, copyright 2024. (j) Schematic of a PRZT battery, (k) dual function of photoelectrode, and (l) GCD curve at (a) 100 mA g^{-1}.[92] Reproduced from ref. 92 with permission from American Chemical Society, copyright 2023.

increased Te loading and exposed more active sites, significantly improving the kinetics of Te redox reactions and reducing the reaction energy barrier. An additional report from the same group reported the development of MoO_2 nanoclusters embedded in nitrogen-doped carbon nanoflower (MoO_2/NC) (Fig. 10f), which were loaded with Te.[89] This structure, with a large specific surface area, enhanced the Te electrochemical kinetics and resulted in superior cycling stability and a high specific capacity of 493 mA h g^{-1}. The use of catalytic molybdenum diselenide-reduced graphene oxide ($MoSe_2$@rGO) hybrids has also been shown to enhance the Te redox reaction kinetics, further improving performance.[90]

Zhu's group reported a $NiTe_2$ nanosheet cathode using mechanical exfoliation, yielding an average lateral size of ~800 nm and a thickness of ~10 nm (Fig. 10g).[91] These nanosheets significantly reduced ion diffusion lengths with plenty of active sites, improving the redox conversion. The electrochemical studies in $ZnSO_4$ electrolyte demonstrated a capacity of 510 mA h g^{-1} at 50 mA g^{-1}, maintaining 97.2% capacity over 400 cycles at 2000 mA g^{-1}. This superior performance is attributed to the high specific surface area of the $NiTe_2$ material, which promotes strong ion/electrolyte interactions and provides dimensional confinement for deep conversion. Pouch cell tests at various bending angles also provided stable discharge plateaus, as depicted in Fig. 10h. *Operando* measurements identified a one-step charging pathway (ZnTe → TeO_2) and a two-step discharge pathway (TeO_2 → Te → ZnTe), highlighting robust reversibility. The proposed six-electron deep multiphase conversion reaction mechanism in a mild aqueous electrolyte (pH ~ 5) is illustrated in Fig. 10i.

Beyond efforts to improve reaction kinetics, Li's group designed a photo-rechargeable aqueous zinc–tellurium (Zn–Te) battery that integrates halide perovskite and tellurium.[92] A Janus-jointed photocathode integrating halide perovskite with a tellurium composite electrode provided a unique structure that facilitates efficient photon absorption and charge transfer. This design resulted in a reduced charging voltage and a notable increase in specific capacity under low illumination, demonstrating self-powering capabilities. This photo-rechargeable zinc–tellurium (PRZT) battery (Fig. 10j) enabled photo-assisted recharging, delivering an additional 362 mA h g^{-1} at 100 mA g^{-1}. Furthermore, the photocathode exhibited a specific capacity at 1000 mA g^{-1}, which was 83% higher under illumination compared to dark conditions (Fig. 10l).

Electrolyte modification strategies for Zn–Te batteries

In Zn–Te systems, initial studies primarily relied on simple aqueous electrolytes, such as $ZnSO_4$ and ZnTFS.[79–83,87–90] However, with these simple electrolytes, achieving highly reversible redox conversion with higher electron transfer remains quite challenging. Hence, additive engineering and salt-rich electrolytes (SREs) have been explored to enable multielectron activation and improve cyclic stability. Li *et al.* designed a $ZnCl_2$, acetonitrile (ACN), and glucose (Glu) additive mixture in a $ZnSO_4$ electrolyte, where nucleophilic Cl^- and reductive Glu acted as the 'offensiver' and 'defender', respectively, for the Te^0/Te^{4+} conversion.[82] The Cl^-/Glu co-additive effectively preserved the nucleophilic activation effect of Cl^- on the tellurium conversion, while suppressing the formation of the Cl^- induced, highly diffusing metastable γ-TeO_2 phase. This strategy enabled a deep and highly reversible Te^0/Te^{4+} redox process. As a result, Zn–Te batteries delivered capacities close to the theoretical value and sustained lifetime exceeding 5000 cycles, outperforming conventional electrolyte systems by 15 to 30-fold.

Using SRE systems, Du *et al.* applied a 30 m $ZnCl_2$ electrolyte, which enabled a dendrite-free Zn anode and smooth Zn stripping/plating without the formation of a solid electrolyte interphase.[85] This electrolyte facilitated reversible amphoteric redox conversion by disrupting the hydrogen-bonding network between water molecules and inhibiting water reactivity towards Te^{4+} hydrolysis, as depicted in Fig. 10c. Another report demonstrated a six-electron transfer in a Te cathode, also enabled by a 30 m $ZnCl_2$ electrolyte in a Zn–Te battery.[86] Here, the six-electron transfer process involved Te^{2-} to Te^{4+} conversion *via* Te^0 and Te^{2+} intermediates, mediated by Zn^{2+} cations and Cl^- anions through the reaction ZnTe ↔ Te ↔ $TeCl^+$ ↔ $TeCl_3^+$. However, this system suffered from the dissolution of Te^{n+} species. To mitigate this issue, 1-butyl-3-methylimidazolium chloride (BMIMCl) : $ZnCl_2$ (1 : 1.2) and BMIMCl : ethylene glycol (EG) : $ZnCl_2$ (1 : 0.3 : 1.2) electrolytes were introduced, enabling high areal capacity under high Te mass loading, while maintaining high energy density and a very low self-discharge rate.

Conclusion and perspective

This review has comprehensively summarized the current state of Se and Te cathode research, systematically analyzing their design, performance, and energy storage mechanisms in aqueous zinc batteries. Se and Te cathodes have recently emerged as compelling alternatives to conventional cathodes for AZIBs. They integrate the high theoretical capacity, superior electronic conductivity, and multielectron conversion chemistry of Se/Te. The combination of these cathode materials with the intrinsic merits of Zn metal anodes, which offer high safety, abundance, energy density, and cost-effectiveness, holds great promise for the development of next-generation high-capacity AZIBs with superior battery performance. In particular, Se offers a judicious balance between relatively high theoretical capacity and electrical conductivity, which can outperform sulfur. Te provides even higher intrinsic conductivity and volumetric energy density, making it particularly suited for high-power and compact energy storage systems. Despite these advantages, both Se- and Te-based AZIBs face persistent barriers and several critical challenges. These include dissolution issues and shuttling of polyselenide/polytelluride intermediates, sluggish conversion kinetics, substantial volume variation during cycling, and the instability of the Zn anode in aqueous electrolytes. Beyond these technical limitations, the toxicity of Se at elevated concentrations and the relative scarcity and high cost of Te present further constraints on their

widespread adoption as cathode materials in AZIBs. However, Se and Te cathodes remain attractive in specific scenarios due to their superior electronic conductivity, remarkable volumetric and gravimetric capacities, and multi-electron transfer redox chemistry. Their multistep redox processes enable both high energy densities and fast kinetics, making them highly attractive for high-performance AZIBs. However, large-scale or low-cost deployment requires careful consideration of material cost, toxicity, and environmental impact. These challenges may be mitigated through strategies such as reducing material loading, improving encapsulation, and implementing recycling approaches. With continued innovations, significant opportunities exist for developing more reliable zinc batteries with Se and Te cathodes. The following future research roadmap is outlined to support and accelerate the advancement of these materials and technologies and to achieve high performance in Zn–Se and Zn–Te batteries.

Cathode design and structural engineering strategies

Both Se and Te exhibit conversion-type redox chemistry, which is accompanied by dissolution of intermediate polyselenides/polytellurides and large volume fluctuations. To overcome these issues, the following cathode designs and architectures are advised. These strategies collectively provide a rational framework for designing high-performance Se- and Te-based cathodes with improved stability, conductivity, and electrochemical reversibility.

(i) *Conducting and porous hosts*: embedding Se/Te into porous carbon matrix, such as hollow carbons, carbon nanotubes, graphene networks, will ensure improvement in conductivity, as well as buffer mechanical stress by providing physical confinement against dissolution. Hierarchical and core–shell structures can also help to mitigate volume expansion problems while maintaining efficient ion/electron transport.

(ii) *Frameworks and polymer composites*: metal–organic frameworks (MOFs), covalent-organic frameworks (COFs), and conducting polymers containing polar functional groups can be introduced to chemically bond Se/Te to enhance the stability of Se/Te-based cathodes and reduce active material loss during cycling.

(iii) *Polar and catalytic hosts*: metal oxides, MXenes, sulfides, and single-atom catalysts can chemically anchor selenide/telluride intermediates (Se^{2-}, Te^{2-}) through strong host–guest interaction. These host materials can facilitate multielectron redox conversion and simultaneously catalyze their reversible conversion reactions. This strategy might also be beneficial for improving reaction kinetics and minimizing irreversible capacity loss.

Electrolyte engineering

Electrolytes play a critical role in governing Se/Te redox chemistry and zinc anode stability. To date, most reports have employed relatively low concentrations of zinc sulfate and zinc trifluoromethanesulfonate salts. However, the following future optimizations can be used to elevate electrochemical properties. These electrolyte strategies collectively provide a versatile approach to improve Se- and Te-based AZIB performance, addressing both cathode stability and zinc anode durability.

(i) *High-concentration or water-in-salt electrolytes (WiSE)*: highly concentrated/WiSE electrolytes are known to reduce water activity, expanding the electrochemical window and potentially suppressing solubility of polyselenide/polytelluride intermediates. Their implementation in Zn–Se and Zn–Te batteries can improve both their interfacial and cyclic stability.

(ii) *Additives and hybrid systems*: organic additives, surfactants, chelating agents, and additional redox mediators can help re-oxidize dissolved Se/Te intermediates back to the cathode, regulate solubility, and modify interface chemistry. Additives can also take part in the formation of the solid electrolyte interphase (SEI). Moreover, additives with specific functional groups can tailor zinc ion solvation sheath and control local pH, improving ionic mobility and transport. Incorporating mixtures of water and organic solvents in controlled ratios, or limited amounts of ionic liquids, can further suppress cathode dissolution while extending the electrochemical potential window.

(iii) *Polymer gel electrolytes*: the use of polymer-based or hydrogel electrolytes can reduce hydrogen evolution and zinc corrosion at the anode and improve interfacial stability. Gel-state electrolytes can also facilitate the development of flexible battery applications.

Zinc anode stabilization

A zinc metal anode is prone to dendrite growth and corrosive side reactions, which significantly reduce the battery's lifespan. Selenium (Se) and tellurium (Te) cathodes can indeed influence the cycling stability of the zinc (Zn) anode in zinc-ion batteries, primarily by forming soluble reaction intermediates that migrate through the electrolyte. During the electrochemical conversion of Se or Te, a range of soluble polyselenide and polytelluride species (such as Se_2^{2-}, Se_4^{2-}, Te_2^{2-}, Te_4^{2-}) can form and dissolve in the aqueous electrolyte. These species can migrate to the zinc metal anode, where they can undergo parasitic chemical or electrochemical reduction reactions. This undesired deposition of foreign Se/Te species on the Zn surface disrupts uniform Zn^{2+} stripping and plating, and induces localized electric-field inhomogeneity, which deteriorates Zn surface morphology and accelerates dendrite formation at the anode. Beyond this, dissolved species can also alter local electrolyte chemistry by modifying pH, ionic speciation, and redox balance, all of which regulate hydrogen evolution and the electrochemical stability window in aqueous electrolytes. Collectively, these interactions lead to enhanced side reactions, accelerated dendrite growth, and ultimately poorer long-term stability of the Zn anode. To mitigate these problems, the following strategies should be implemented. These approaches will enhance anode stability and contribute to longer cycle life in zinc-based batteries.

(i) *Artificial SEI layers*: creating innovative artificial SEI layers can play a key role in optimizing interfacial ion transport and in boosting battery performance and prolonging cycle life through improved interfacial stability. Coatings composed of organic

molecules, polymers, ceramics, or hybrid layers can form stable solid electrolyte interphases (SEI) and suppress dendrite growth or reduce zinc corrosion.

(ii) *3D current collectors*: porous zinc hosts can promote more uniform current distribution, lowering local current density and enabling uniform zinc deposition.

Mechanistic insights and advanced characterization methods

The redox chemistry of Se/Te is inherently complex. It involves multiple electrons and the formation of intermediate phases during the battery cycling process. A thorough understanding of these mechanisms is key to rational design.

(i) *Operando/in situ techniques*: X-ray diffraction (XRD), Raman spectroscopy, and X-ray absorption spectroscopy (XAS) can be employed to monitor the formation of intermediate species in real time during battery operation. These approaches can be complemented by advanced *ex situ* microscopic characterization techniques, such as transmission electron microscopy (TEM) and scanning electron microscopy (SEM), to visualize structural changes and volume expansion. Additionally, an Electrochemical quartz crystal microbalance (EQCM) can be used to track mass changes and dissolution dynamics.

(ii) *Computational modeling*: computational modeling plays a crucial role in battery research by providing atomic- and molecular-level insights, predicting material behavior, and guiding the design of high-performance electrode and electrolyte systems. Density functional theory (DFT) and molecular dynamics (MD) methods can predict binding energies of intermediates with various hosts, elucidate solvation structures, and estimate reaction kinetics, thereby supporting a mechanistic understanding.

Prospects for practical applications

Zn–Se and Zn–Te batteries represent a compelling option for applied research due to their low cost and ambient stability. However, most currently available cathode materials fall short of meeting the essential performance requirements of practical batteries. Consequently, hybrid battery systems offer the most viable pathway for near-term commercialization, while long-term progress will rely on fundamental research to enable the development of fully optimized battery systems. For Se/Te cathodes to transition from lab-scale proof-of-concept to real-world applications, the following points need to be considered.

(i) *Capacity, cycling performance, and scalability*: batteries should deliver high areal capacity and energy density while employing simple and reproducible fabrication methods. Long-term cycling stability must be demonstrated under realistic current densities and mass loadings. Cost-effective synthesis of Se/Te composites and printable or flexible electrode architectures should be prioritized to facilitate scalable production, enhance value, and support novel applications.

(ii) *Safety and environmental concerns*: selenium exhibits moderate toxicity, and tellurium is relatively scarce. Hence, future studies should incorporate recycling strategies and comprehensive life-cycle assessments to ensure environmental sustainability and safe deployment of these materials.

Author contributions

Hiren K. Machhi: conceptualization, literature search; data curation; writing – original draft, editing, visualization (figures/tables). Jiri Cervenka: conceptualization, funding acquisition, supervision, writing – review & editing; project administration, resources.

Conflicts of interest

The authors declare no conflict of interest.

Data availability

Data for this article, including descriptions of data types, are available at Zenodo at https://doi.org/10.5281/zenodo.17289544.

Supplementary information (SI): Pourbaix diagrams of important Se and Te materials. See DOI: https://doi.org/10.1039/d5ta08186f.

Acknowledgements

We gratefully acknowledge the support of the Czech Science Foundation (GAČR Project No. 24-10535K). This work was also funded by the Programme Johannes Amos Comenius financed by the European Union and the Czech Ministry of Education, Youth and Sports, as part of the AMULET project (CZ.02.01.01/00/22_008/0004558).

References

1 X. Zeng, M. Li, D. Abd El-Hady, W. Alshitari, A. S. Al-Bogami, J. Lu and K. Amine, *Adv. Energy Mater.*, 2019, **9**, 1900161.
2 H. Sun, B. Chen, M. Tan, Y. Li, X. Lang and Q. Jiang, *J. Mater. Chem. A*, 2025, **13**, 17159–17196.
3 G. Li, L. Sun, S. Zhang, C. Zhang, H. Jin, K. Davey, G. Liang, S. Liu, J. Mao and Z. Guo, *Adv. Funct. Mater.*, 2024, **34**, 2301291.
4 A. Hashem Abdelmohsen, S. A. El-khodary, N. Ismail, Z. Song and J. Lian, *Chem.–Eur. J.*, 2025, **31**, e202403425.
5 K. Zhu and W. Yang, *Acc. Chem. Res.*, 2024, **57**, 2887–2900.
6 Y. Li, J. Zhao, Q. Hu, T. Hao, H. Cao, X. Huang, Y. Liu, Y. Zhang, D. Lin, Y. Tang and Y. Cai, *Mater. Today Energy*, 2022, **29**, 101095.
7 P. M. Hari Prasad, G. Malavika, A. Pillai, S. Sadan and Z. S. Pillai, *NPG Asia Mater.*, 2024, **16**, 37.
8 Z. Yan, Q. H. Yang and C. Yang, *J. Mater. Chem. A*, 2024, **12**, 24746–24760.
9 K. K. Sonigara, J. Zhao, H. K. Machhi, G. Cui and S. S. Soni, *Adv. Energy Mater.*, 2020, **10**, 2001997.
10 A. Mahmood, Z. Zheng and Y. Chen, *Adv. Sci.*, 2024, **11**, 2305561.
11 J. Zhang, M. Shi, X. Ren, C. Wu, S. Hu, J. Feng, G. Li and C. Peng, *J. Energy Storage*, 2024, **88**, 111604.

12 H. Zhao, L. Zhao, D. Yin, N. Gao, Y. Zhang, J. Feng, X. Chen, X. Liu, J. Wei, C. Fan, G. Gao, C. Xiao and S. Ding, *Adv. Mater.*, 2025, e15759, DOI: 10.1002/adma.202515759.
13 R. Ajay Rakkesh, S. Shalini, S. Tharani, D. Durgalakshmi and S. Balakumar, *Energy Adv*, 2024, **3**, 676–688.
14 J. Xu, J. Ma, Q. Fan, S. Guo and S. Dou, *Adv. Mater.*, 2017, **29**, 1606454.
15 M. Mansuer, L. Miao, Y. Qin, Z. Song, D. Zhu, H. Duan, Y. Lv, L. Li, M. Liu and L. Gan, *Chin. Chem. Lett.*, 2023, **34**, 107304.
16 W. Du, Z. Song, X. Zheng, Y. Lv, L. Miao, L. Gan and M. Liu, *ChemSusChem*, 2024, **17**, e202400886.
17 H. Xu, W. Yang, M. Li, H. Liu, S. Gong, F. Zhao, C. Li, J. Qi, H. Wang, W. Peng and J. Liu, *Small*, 2024, **20**, 2310972.
18 Y. Zhao, J. Zhu, C. Li, S. Zhang, R. Zhang, P. Li, H. Hong, Q. Nian, H. Lv and C. Zhi, *J. Mater. Chem. C*, 2024, **12**, 14809–14815.
19 J. Liu, W. Zhou, R. Zhao, Z. Yang, W. Li, D. Chao, S. Z. Qiao and D. Zhao, *J. Am. Chem. Soc.*, 2021, **143**(38), 15475–15489.
20 X. Liu, Y. Li, X. Xu, L. Zhou and L. Mai, *J. Energy Chem.*, 2021, **61**, 104–134.
21 M. Han, L. Qin, Z. Liu, L. Zhang, X. Li, B. Lu, J. Huang, S. Liang and J. Zhou, *Mater. Today Energy*, 2021, **20**, 100626.
22 D. Selvakumaran, A. Pan, S. Liang and G. Cao, *J. Mater. Chem. A*, 2019, **7**, 18209–18236.
23 S. Jia, L. Li, Y. Shi, C. Wang, M. Cao, Y. Ji and D. Zhang, *Nanoscale*, 2024, **16**, 1539–1576.
24 Y. Zhang, E. H. Ang, K. N. Dinh, K. Rui, H. Lin, J. Zhu and Q. Yan, *Mater. Chem. Front.*, 2021, **5**, 744–762.
25 S. S. Shiam, J. Rath and A. Kiani, *Int. J. Electrochem. Sci.*, 2024, **19**, 100804.
26 G. Li, Z. Yang, Y. Jiang, C. Jin, W. Huang, X. Ding and Y. Huang, *Nano Energy*, 2016, **25**, 211–217.
27 D. Singh, Y. Hu, S. S. Meena, R. Vengarathody, M. Fichtner and P. Barpanda, *Chem. Commun.*, 2023, **59**, 14391–14394.
28 W. Li, K. Wang, S. Cheng and K. Jiang, *Energy Storage Mater.*, 2018, **15**, 14–21.
29 A. Kim, Y. Park, J. Choi, S. H. Yu and K. W. Nam, *ACS Appl. Energy Mater.*, 2025, **8**(11), 6806–6828.
30 X. Wang, Z. Zhang, B. Xi, W. Chen, Y. Jia, J. Feng and S. Xiong, *ACS Nano*, 2021, **15**(6), 9244–9272.
31 L. Long, K. Mei, Z. Hou, Y. Wang, H. Zhang and W. Sun, *Nanoscale Horiz.*, 2025, **10**, 2340–2364.
32 C. Hu, X. Yang, P. Liu, Z. Song, Y. Lv, L. Miao, M. Liu and L. Gan, *J. Mater. Chem. A*, 2024, **12**, 11867–11874.
33 K. Hua, Q. Ma, Y. Liu, P. Xiong, R. Wang, L. Yuan, J. Hao, L. Zhang and C. Zhang, *ACS Nano*, 2025, **19**, 14249–14261.
34 X. Chen, J. H. Liu, H. Jiang, C. Zhan, Y. Gao, J. Li, H. Zhang, X. Cao, S. Dou and Y. Xiao, *Energy Storage Mater.*, 2024, **65**, 103168.
35 L. Zhu, Q. Shao, C. Zhang, X. Cao, D. Liu, C. Zhi and D. Wang, *Energy Storage Mater.*, 2024, **67**, 103297.
36 T. Chowdhury, E. C. Sadler and T. J. Kempa, *Chem. Rev.*, 2020, **120**(22), 12563–12591.
37 S. Li, X. Zhao, T. Wang, J. Wu, X. Xu, P. Li, X. Ji, H. Hou, X. Qu, L. Jiao and Y. Liu, *Angew. Chem., Int. Ed.*, 2024, **63**, e202320075.
38 A. A. Altalhi, E. A. Mohamed and N. A. Negm, *Energy Adv*, 2024, **3**, 2136–2151.
39 B. Qin, X. Feng, Z. Feng and Z. Zhang, *Energy Storage Mater.*, 2025, **81**, 104454.
40 S. Jangra, B. Kumar, J. Sharma, S. Sengupta, S. Das, R. K. Brajpuriya, A. Ohlan, Y. K. Mishra and M. S. Goyat, *J. Energy Storage*, 2024, **101**, 113810.
41 Y. Shen, H. Lv and L. Chen, *Mater. Chem. Front.*, 2023, **7**, 2373–2404.
42 H. Wen, H. Wen, Y. Sun, J. Li, C. Zhuang, M. Liu, H. Li, H. Fan, B. Yin, S. Zhang and T. Ma, *Adv. Funct. Mater.*, 2025, **35**, 2500323.
43 A. Iqbal, O. M. El-Kadri and N. M. Hamdan, *J. Energy Storage*, 2023, **62**, 106926.
44 Q. Wang, S. Kaushik, X. Xiao and Q. Xu, *Chem. Soc. Rev.*, 2023, **52**, 6139–6190.
45 C. Feng, X. Jiang, Q. Zhou, T. Li, Y. Zhao, Z. Niu, Y. Wu, H. Zhou, M. Wang, X. Zhang, M. Chen, L. Ni, G. Diao and Y. Wei, *J. Mater. Chem. A*, 2023, **11**, 18029–18045.
46 B. Lu, J. Deng, Z. Wu, H. Yu, L. Yan, L. Zhang, T. F. Yi and J. Shu, *Adv. Mater.*, 2025, **37**, 2505203.
47 V. S. Saji and C. W. Lee, *RSC Adv.*, 2013, **3**, 10058–10077.
48 B. Lange and M. G. Van Den Berg, *Anal. Chim. Acta*, 2000, **418**, 33–42.
49 R. Piech and W. W. Kubiak, *Electrochim. Acta*, 2007, **53**, 584–589.
50 X. Gu, T. Tang, X. Liu and Y. Hou, *J. Mater. Chem. A*, 2019, **7**, 11566–11583.
51 Z. Chen, F. Mo, T. Wang, Q. Yang, Z. Huang, D. Wang, G. Liang, A. Chen, Q. Li, Y. Guo, X. Li, J. Fan and C. Zhi, *Energy Environ. Sci.*, 2021, **14**, 2441–2450.
52 A. Kathalingam, T. Mahalingam and C. Sanjeeviraja, *Mater. Chem. Phys.*, 2007, **106**, 215–221.
53 X. Wu, X. Chen, Y. Yan, G. Diao, H. Yan, L. Ni, Y. Piao and M. Chen, *Adv. Sci.*, 2024, **11**, 2403224.
54 P. Li, Y. Wang and C. Zhi, *Batteries Supercaps*, 2025, **8**, e202400327.
55 Z. Jiang, X. Yang, J. Zhang, J. Yang, B. Sun, Z. Sun, J. Xue, J. He, Z. Sun, H. K. Liu and S. X. Dou, *Adv. Funct. Mater.*, 2025, **35**, e11754.
56 J. Du, J. Zhang, X. Chu, H. Xu, Y. Zhao, M. Löffler, G. Wang, D. Li, Q. Guo, A. Morag, J. Du, J. Zou, D. Mikhailova, V. Mazánek, Z. Sofer, X. Feng and M. Yu, *Nat. Commun.*, 2025, **16**, 3707.
57 C. Dai, L. Hu, H. Chen, X. Jin, Y. Han, Y. Wang, X. Li, X. Zhang, L. Song, M. Xu, H. Cheng, Y. Zhao, Z. Zhang, F. Liu and L. Qu, *Nat. Commun.*, 2022, **13**, 1863.
58 J. Wang and W. Q. Han, *Adv. Funct. Mater.*, 2022, **32**, 2107166.
59 F. Cui, R. Pan, L. Su, C. Zhu, H. Lin, R. Lian, R. Fu, G. Zhang, Z. Jiang, X. C. Hu, Y. Pan, S. Hou, F. Zhang, K. Zhu, Y. Dong and F. Xu, *Adv. Mater.*, 2023, **35**, 2306580.
60 H. Xu, S. Fan, H. Liu, P. Guo, N. Ji, C. Li, H. Wang, W. Peng, X. Fan and J. Liu, *Energy Storage Mater.*, 2025, **82**, 104604.
61 T. Bai, D. Li, S. Xiao, F. Ji, S. Zhang, C. Wang, J. Lu, Q. Gao and L. Ci, *Energy Environ. Sci.*, 2023, **16**, 1431–1465.

62 Y. Wang, F. Chu, J. Zeng, Q. Wang, T. Naren, Y. Li, Y. Cheng, Y. Lei and F. Wu, *ACS Nano*, 2021, **15**(1), 210–239.
63 Z. Zhang, J. Dong, C. Huang, K. Wan, Z. Feng, B. Li, N. Zhao, L. Dai, L. Wang and Z. He, *Chem. Eng. J.*, 2025, **506**, 159958.
64 H. Xu, P. Guo, C. Li, J. Gao, H. Wang, W. Peng and J. Liu, *Adv. Funct. Mater.*, 2025, **35**, 2415016.
65 D. Jin, M. R. Krumov, R. M. Mandel, P. J. Milner and H. D. Abruña, *ACS Energy Lett.*, 2024, **9**, 5822–5829.
66 L. Ma, Y. Ying, S. Chen, Z. Chen, H. Li, H. Huang, L. Zhao and C. Zhi, *Adv. Energy Mater.*, 2022, **12**, 2201322.
67 A. Anjan, M. Mahato, K. Bhimani, A. K. Kushwaha, V. Mahajani, H. Yoo, R. A. Panchal, R. M. Manoj, J. Ha, S. K. Nayak, P. Keblinkski, I. K. Oh and N. Koratkar, *Adv. Funct. Mater.*, 2024, **34**, 2410225.
68 Y. Zhang, Y. Li, S. Yao, N. Ali, X. Kong and J. Wang, *Energy Storage Mater.*, 2024, **71**, 103544.
69 J. Y. Zhang, L. B. Kong, L. Z. Zhan, J. Tang, H. Zhan, Y. H. Zhou and C. M. Zhan, *J. Power Sources*, 2007, **168**, 278–281.
70 Z. Huang, Y. Hou, T. Wang, Y. Zhao, G. Liang, X. Li, Y. Guo, Q. Yang, Z. Chen, Q. Li, L. Ma, J. Fan and C. Zhi, *Nat. Commun.*, 2021, **12**, 3106.
71 Z. Chen, H. Cui, Y. Hou, X. Wang, X. Jin, A. Chen, Q. Yang, D. Wang, Z. Huang and C. Zhi, *Chem*, 2022, **8**, 2204–2216.
72 J. Yan, B. Wang, Y. Tang, W. Du, M. Ye, Y. Zhang, Z. Wen, X. Liu and C. C. Li, *Angew. Chem., Int. Ed.*, 2024, **63**, e202400121.
73 Z. Chen, Y. Hou, Y. Wang, Z. Wei, A. Chen, P. Li, Z. Huang, N. Li and C. Zhi, *Adv. Mater.*, 2024, **36**, 2309330.
74 J. Wei, P. Zhang, J. Sun, Y. Liu, F. Li, H. Xu, R. Ye, Z. Tie, L. Sun and Z. Jin, *Chem. Soc. Rev.*, 2024, **53**, 10335–10369.
75 S. Liu, Y. Liao, T. Liu, L. Chen and Q. Zhang, *Energy Storage Mater.*, 2024, **73**, 103799.
76 Z. Khan, D. Kumar and X. Crispin, *Adv. Mater.*, 2023, **35**, 2300369.
77 Y. Zhang, D. Manaig, D. J. Freschi and J. Liu, *Energy Storage Mater.*, 2021, **40**, 166–188.
78 Y. Zhang and J. Liu, *Acc. Chem. Res.*, 2024, **57**, 2500–2511.
79 Z. Chen, Q. Yang, F. Mo, N. Li, G. Liang, X. Li, Z. Huang, D. Wang, W. Huang, J. Fan and C. Zhi, *Adv. Mater.*, 2020, **32**, 2001469.
80 M. Kim, H. Kim, S. H. Lee, S. Yu, W. Kim, J. S. Bae, C. Y. Ahn, H. Shim, J. E. Lee and S. H. Yu, *Chem. Eng. J.*, 2024, **481**, 148256.
81 J. Wang, J. Du, J. Zhao, Y. Wang, Y. Tang, G. Cui and J. Physical, *Chem. Lett.*, 2021, **12**, 10163–10168.
82 J. Qi, Y. Tang, Z. Feng, J. Yan, G. Liu, M. Ye, W. Du, Q. Yang, Y. Wei, Y. Zhang, Z. Wen, X. Liu and C. C. Li, *Adv. Energy Mater.*, 2024, **14**, 2303616.
83 Z. Yan, J. Li, H. Liu, H. Zhang, S. Xi and Z. Zhu, *Angew. Chem., Int. Ed.*, 2023, **62**, e202312000.
84 C. Guo, S. Yi, R. Si, Y. Wang, H. Liu, F. Yu and J. Li, *Chem. Eng. J.*, 2023, **469**, 143845.
85 J. Du, Y. Zhao, X. Chu, G. Wang, C. Neumann, H. Xu, X. Li, M. Löffler, Q. Lu, J. Zhang, D. Li, J. Zou, D. Mikhailova, A. Turchanin, X. Feng and M. Yu, *Adv. Mater.*, 2024, **36**, 2313621.
86 Z. Chen, S. Wang, Z. Wei, Y. Wang, Z. Wu, Y. Hou, J. Zhu, Y. Wang, G. Liang, Z. Huang, A. Chen, D. Wang and C. Zhi, *J. Am. Chem. Soc.*, 2023, **145**, 20521–20529.
87 H. Xu, W. Yang, H. Liu, M. Li, S. Gong, F. Zhao, C. Li, J. Qi, H. Wang, W. Peng, X. Fan and J. Liu, *Chem. Eng. J.*, 2023, **465**, 142896.
88 H. Xu, H. Liu, W. Yang, M. Li, F. Zhao, C. Li, J. Qi, H. Wang, W. Peng, X. Fan and J. Liu, *Chem. Eng. J.*, 2024, **485**, 149825.
89 H. Wang, W. Yang, H. Xu, M. Li, H. Liu, S. Gong, F. Zhao, C. Li, J. Qi, W. Peng and J. Liu, *Small*, 2023, **19**, 2304504.
90 G. Gu, J. Wen, H. Xu, Y. Zhang, M. Li, H. Zhai, W. Yang, C. Li, H. Wang, W. Peng and J. Liu, *J. Energy Storage*, 2024, **88**, 111672.
91 J. Si, Y. Sun, R. Qi, Q. Lei, W. Zhang, Z. Ren, Y. Zhao, H. Li, M. Lin, W. Wen, J. Zhang, Z. Feng, Y. Gao, X. Li and D. Zhu, *Adv. Energy Mater.*, 2024, **14**, 2303982.
92 H. Liu, P. Wu, R. Wang, H. Meng, Y. Zhang, W. Bao and J. Li, *ACS Nano*, 2023, **17**, 1560–1569.
93 M. Kim, H. Y. Choi and S. H. Yu, *Chem. Eng. J.*, 2025, **504**, 158528.